LRRK2 regulates innate immune responses and neuroinflammation during *Mycobacterium tuberculosis* infection

C.G. Weindel[1*], S.L. Bell[1*], T. Huntington[3], K. Vail[2], R. Srinivasan[3], K.L. Patrick[1], R.O. Watson[1]

[1]Department of Microbial Pathogenesis and Immunology, Texas A&M Health Science Center, TX, 77807, USA

[2]Department of Veterinary Pathobiology, Texas A&M University College of Veterinary Medicine and Biomedical Sciences, 77843 USA

[3]Department of Neuroscience and Experimental Therapeutics, Texas A&M Health Science Center, TX, 77807, USA

*these authors contributed equally

Correspondence: robert.watson@medicine.tamhsc.edu
Phone: (979) 436-0342

SUMMARY

Despite many connections between mutations in leucine-rich repeat kinase 2 (*LRRK2*) and susceptibility to mycobacterial infection, we know little about its function outside of the brain, where it is studied in the context of Parkinson's Disease (PD). Here, we report that Lrrk2 controls peripheral macrophages and brain-resident glial cells' ability to respond to and express inflammatory molecules. *LRRK2* KO macrophages express elevated basal levels of type I interferons, resulting from defective purine metabolism, mitochondrial damage, and engagement of mitochondrial DNA with the cGAS DNA sensing pathway. While *LRRK2* KO mice can control *Mycobacterium tuberculosis* (Mtb) infection, they exhibit exacerbated lung inflammation and altered activation of glial cells in PD-relevant regions of the brain. These results directly implicate Lrrk2 in peripheral immunity and support the "multiple-hit hypothesis" of neurodegenerative disease, whereby infection coupled with genetic defects in *LRRK2* create an immune milieu that alters activation of glial cells and may trigger PD.

INTRODUCTION

Mutations in leucine rich repeat kinase 2 (*LRRK2*) are a major cause of familial and sporadic Parkinson's Disease (PD), a neurodegenerative disease characterized by selective loss of dopaminergic (DA) neurons in the substantia nigra pars compacta (SNc) region of the midbrain (Cookson, 2017; Kim and Alcalay, 2017; Martin et al., 2014; Schulz et al., 2016). Despite Lrrk2 having been implicated in a variety of cellular processes including cytoskeletal dynamics (Civiero et al., 2018; Kett et al., 2012; Pellegrini et al., 2017), vesicular trafficking (Herbst and Gutierrez, 2019; Sanna et al., 2012; Shi et al., 2017), calcium signaling (Bedford et al., 2016; Calì et al., 2014), and mitochondrial function (Ryan et al., 2015; Singh et al., 2019; Yue et al., 2015), its precise mechanistic contributions to triggering and/or exacerbating PD are not known.

Of all the cellular pathways affected by *LRRK2* mutations, dysregulation of mitochondrial homeostasis has emerged as a centrally important mechanism underlying PD pathogenesis and neuronal loss (Cowan et al., 2019; Panchal and Tiwari, 2019). Indeed, other PD-associated genes such as *PARK2* (Parkin), *PINK1*, and *DJ1*, all play crucial roles in mitochondrial quality control via mitophagy. Lrrk2 has been implicated in mitophagy directly through interactions with the mitochondrial outer membrane protein Miro (Hsieh et al., 2016), and several lines of evidence support roles for Lrrk2 in controlling mitochondrial network dynamics through interactions with the mitochondrial fission protein Drp1 (X. Wang et al., 2012). Accordingly, a number of different cell types, including fibroblasts and iPSC-derived neurons from PD patients harboring mutations in *LRRK2* exhibit increased oxidative stress, increased ROS, and defects in mitochondrial network integrity (Sison et al., 2018; Smith et al., 2016). Because DA neurons in the SNc have high bioenergetic needs and a unique highly-branched morphology, they are thought to be particularly sensitive to defects in mitochondrial homeostasis conferred by mutations in *LRRK2* (Surmeier et al., 2017). In spite of these well-appreciated links, Lrrk2's contribution to mitochondrial health in cells outside of the brain remains vastly understudied.

There is mounting evidence that mutations in *LRRK2* contribute to immune outcomes both in the brain and in the periphery. For example, mutations in *LRRK2* impair NF-κB pathways in iPSC-derived neurons and render rats prone to progressive neuroinflammation following administration of peripheral innate immune triggers (López de Maturana et al., 2016). Likewise, chemical inhibition of *LRRK2* attenuates inflammatory responses in microglia *ex vivo* (Moehle et al., 2012). In addition to these strong connections between *LRRK2* and inflammatory responses in the brain, numerous GWAS studies suggest that *LRRK2* is an equally important player in the

peripheral immune response. Numerous single nucleotide polymorphisms (SNPs) in *LRRK2* are associated with susceptibility to mycobacterial infection (Fava et al., 2016; Marcinek et al., 2013; D. Wang et al., 2015; F.-R. Zhang et al., 2009), inflammatory colitis (Umeno et al., 2011), and Crohn's Disease (Van Limbergen et al., 2009). Consistent with a role for *LRRK2* in pathogen defense and autoimmunity, *LRRK2* is abundant in many immune cells (e.g. B cells, dendritic cells, monocytes, macrophages) and expression of *Lrrk2* is induced in human macrophages treated with IFN-γ (Gardet et al., 2010). Loss of *LRRK2* reduces IL-1β secretion in response to *Salmonella enterica* infection in macrophages *ex vivo* (Liu et al., 2017) and enhances expression of pro-inflammatory cytokines in response to Mtb infection (Härtlova et al., 2018). However, the precise mechanistic contribution(s) of *LRRK2* to controlling immune responses in the periphery remain poorly understood.

Here, we provide the first evidence that *LRRK2*'s ability to influence inflammatory gene expression in macrophages is directly linked to its roles in maintaining mitochondrial homeostasis. Specifically, we demonstrate that depolarization of the mitochondrial network and hyper-activation of Drp1 in *LRRK2* KO macrophages leads to release of mtDNA, engagement of the cGAS-dependent DNA sensing pathway, and abnormally high basal levels of interferon β (type I interferon (IFN)) and interferon stimulated genes (ISGs). These high basal levels of type IFN appears to completely reprogram *LRRK2* KO macrophages, rendering them refractory to a number of distinct innate immune stimuli, including infection with the important human lung pathogen, Mtb. While Mtb-infected *LRRK2* KO mice did not exhibit significant differences in bacterial burdens, we did observe exacerbated pathology in the lungs. Remarkably, although no bacilli were present in the brains of CT or KO mice, both exhibited dramatic signs of neuroinflammation, evidenced by activation of microglia and astrocytes in the dorsolateral striatum (DLS), a PD-relevant region of the brain. Collectively, these results (1) demonstrate that *LRRK2*'s role in maintaining mitochondrial homeostasis is critical for proper induction of inflammatory gene expression in both peripheral macrophages and brain-resident glial cells and (2) provide strong support for the "multiple-hit hypothesis" of neurodegeneration, whereby peripheral infection coupled with specific genetic mutations may trigger or exacerbate neuronal loss.

RESULTS

RNA-SEQ analysis reveals that *LRRK2* deficiency in macrophages results in dysregulation of the type I interferon response following Mtb infection

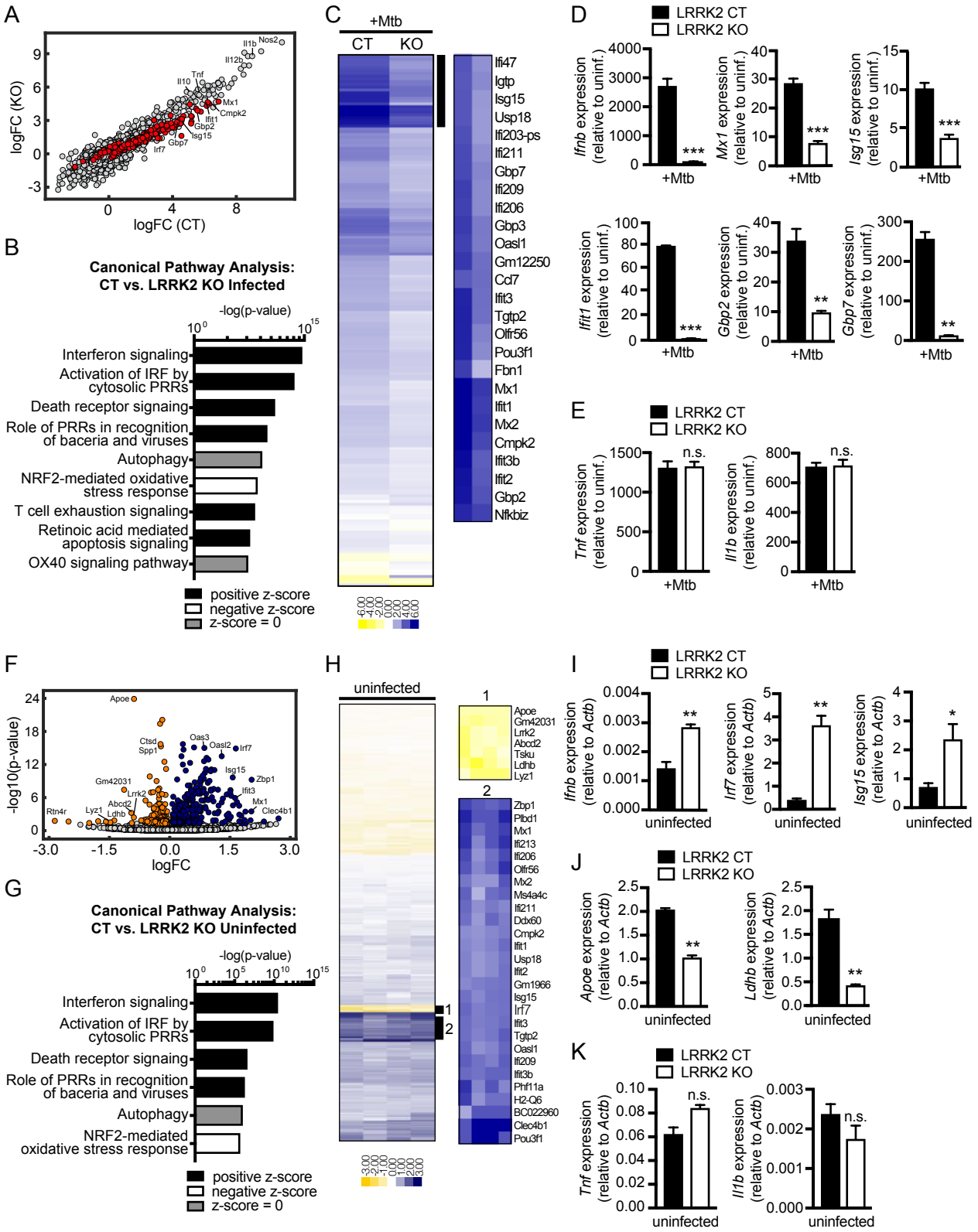

Figure 1. Global gene expression analysis reveals that LRRK2 KO macrophages are deficient at inducing type I IFN expression and have higher basal levels of type I IFN stimulated genes (A) Scatter plot of genes up- and down-regulated in LRRK2 KO and Control (CT) BMDMs following 4hrs of infection with Mtb. Genes whose expression changes are significant ($p<0.001$; adjusted p value is $p<0.05$) are highlighted in red. (B) IPA software analysis showing cellular pathways enriched for differentially expressed genes in LRRK2 KO vs. CT BMDMs during Mtb infection. (C) Heatmap depicting significant gene expression differences (Log2 fold-change) between LRRK2 KO and CT BMDMs during infection with Mtb. (D) RT-qPCR showing mRNA fold change of type I IFN associated genes Ifnb, Mx1, Isg15, and type II IFN genes Ifit1, Gbp2, Gbp7 during infection with Mtb. (E) RT-qPCR of NFκB genes Tnf and IL1b during infection with Mtb. (F) Volcano plot depicting the distribution of genes significantly upregulated (blue) or downregulated (orange) upon loss of LRRK2 in uninfected (resting) BMDMs. (G) As in (B) but between uninfected LRRK2 KO and CT BMDMs. (H) As in (C) but for uninfected LRRK2 KO and CT BMDMs. Zoom 1 are top downregulated genes, Zoom 2 are top upregulated genes. (I) RT-qPCR of type I IFN associated genes Ifnb, Irf7, Isg15 normalized to Actb in uninfected BMDMs. (J) RT-qPCR of Apoe and Ldhb normalized to Actb in uninfected BMDMs. (K) Same as (E), but in uninfected BMDMs

To begin to implicate *LRRK2* in the peripheral immune response, we took an unbiased approach to determine how loss of *LRRK2* impacts innate immune gene expression during Mtb infection of macrophages *ex vivo*. Briefly, primary murine bone marrow-derived macrophages (BMDMs) derived from littermate heterozygous (control, CT) and knockout (KO) *LRRK2* mice were infected with Mtb at a MOI=10 and RNA-seq analysis was performed on total RNA collected from uninfected and infected cells 4h post-infection. Previous studies have identified 4h as a key innate immune time point during Mtb infection, corresponding to the peak of transcriptional activation downstream of sensing molecules including the cytosolic DNA sensor cGAS (Manzanillo et al., 2012; Watson et al., 2015; 2012).

Following analysis with CLC Genomics Workbench, we identified hundreds of genes that were differentially expressed in *LRRK2* KO vs. CT BMDMs during Mtb infection, with 192 genes significantly up- or down-regulated (179 up, 13 down) ($p<0.001$) (Fig. 1A, Table S1). Although a number of genes were significantly induced during infection in both genotypes, the level of induction for a number of transcripts was noticeably lower in *LRRK2* KO cells compared to CT (Fig. 1C). Canonical pathway analysis of differentially expressed genes revealed significant enrichment for genes involved in type I IFN and other related pathways (-log(p)=12.98), including Activation of IRF by cytosolic Pattern recognition receptors (-log(p)=11.81), RIG-I signaling (-log(p)=4.69) and autophagy (-log(p)=3.815) (Fig. 1B, S1B). Indeed, a majority of the top differentially expressed genes were well-known interferon-stimulated genes (ISGs), including *Ifit1*, *Mx1*, and *Isg15* (Fig. 1C). Mtb is a potent activator of type I IFN expression, thought to occur mostly through permeabilization of the Mtb-phagosome and release of bacterial dsDNA into the cytosol, where it is detected by DNA sensors like cGAS, activating the STING/TBK1/IRF3 axis (Collins et al., 2015; Wassermann et al., 2015; Watson et al., 2015; Wiens and Ernst, 2016). Follow-up RT-qPCR analysis confirmed that *Ifnb* and ISGs like *Mx1*, *Isg15*, and *Gbp7* were induced to lower levels in *LRRK2* KO macrophages compared to controls following Mtb infection (Fig. 1D). This differential response seemed to be specific for type I IFN and ISGs since the transcripts of Mtb-induced cytokines like *Tnf* and *Il1b* reached similar levels in both genotypes (Fig. 1E).

Resting *LRRK2* KO macrophages express elevated levels of type I IFN

To begin to investigate the nature of this defect in type I IFN induction, we again used CLC Genomics Workbench analysis to identify transcripts affected by loss of *LRRK2* in uninfected or “resting” macrophages. We observed higher basal expression of a number of innate immune transcripts in *LRRK2* KO BMDMs relative to control, including several type I IFN

family genes (e.g. *Oas3*, *Irf7*, *Oasl2*, *Isg15*, *Zbp1*) (Fig. 1F, 1H). Indeed, differential gene expression analysis and unbiased canonical pathways analysis revealed that again, "Interferon Signaling" was the most significantly impacted pathway in resting macrophages (-log(p)=12.95) (Fig. 1G). In fact, almost all the pathways and families of genes that were differentially expressed in *LRRK2* KO BMDMs in *Mtb*-infected cells were also impacted in uninfected cells (Fig. 1B and 1G, S1C-D). RT-qPCR analysis confirmed significantly elevated levels of type I IFN transcripts including *Ifnb*, *Irf7*, *Isg15*, and *Ifit* in *LRRK2* KO BMDMs (Fig. 1I and S1E). Interestingly, several transcripts, including *Apoe*, a gene associated with Alzheimer's and cardiovascular disease, had decreased expression in *LRRK2* KO BMDMs compared to controls (Fig. 1J). Transcripts like *Tnf* were again expressed at similar levels in the two genotypes (Fig. 1K). Importantly, the resting and induced levels of interferon and ISGs were similar between WT and HET *LRRK2* BMDMs, validating our use of HETs as controls in future experiments (Fig. S1F-G).

We also found increased basal expression and decreased induction of interferon and ISGs upon Mtb infection in the human monocyte cell line U937 (Fig. 2A and S2A) and in RAW 264.7 macrophages when *LRRK2* was knocked down by shRNA (Fig. S2C). Infection of RAW 264.7 cells in which *LRRK2* is knocked out (RAW 264.7 *LRRK2* KO) with *Mycobacterium leprae* (Mlep), which shares the virulence-associated ESX-1 secretion system with Mtb and also induces type I IFN through cytosolic nucleic acid sensing (de Toledo-Pinto et al., 2016), showed a similar defect in type I IFN induction compared to CT RAW cells (Fig. 2B and S2B). Together, these transcriptome-focused analyses reveal that *LRRK2* KO macrophages have a higher interferon signature at baseline but are unable to induce the type I IFN response to the same levels as control cells when infected with Mtb or Mlep.

LRRK2 KO macrophages fail to induce type I IFN in response to diverse innate immune stimuli

Because both Mtb and Mlep stimulate type I IFN through the cGAS/STING/TBK1 axis, we hypothesized that loss of *LRRK2* may cause defects in this pathway. Briefly, CT and KO BMDMs were treated with a series of agonists that stimulate a variety of innate immune pathways and elicit a type I IFN response. *LRRK2* KO BMDMs failed to fully induce *Ifnb* and *Irf7* transcripts following transfection of interferon stimulating DNA (ISD) (Fig. 2C), as did *LRRK2* KO peritoneal macrophages (Fig. 2D), *LRRK2* KO or KD RAW macrophages (Fig. 2E and S2C), and *LRRK2* KO MEFs (Fig 2F and S2E). Likewise, stimulating the DNA sensing adapter STING directly using the agonist DMXAA or transfection of the cGAS product/STING agonist, cGAMP

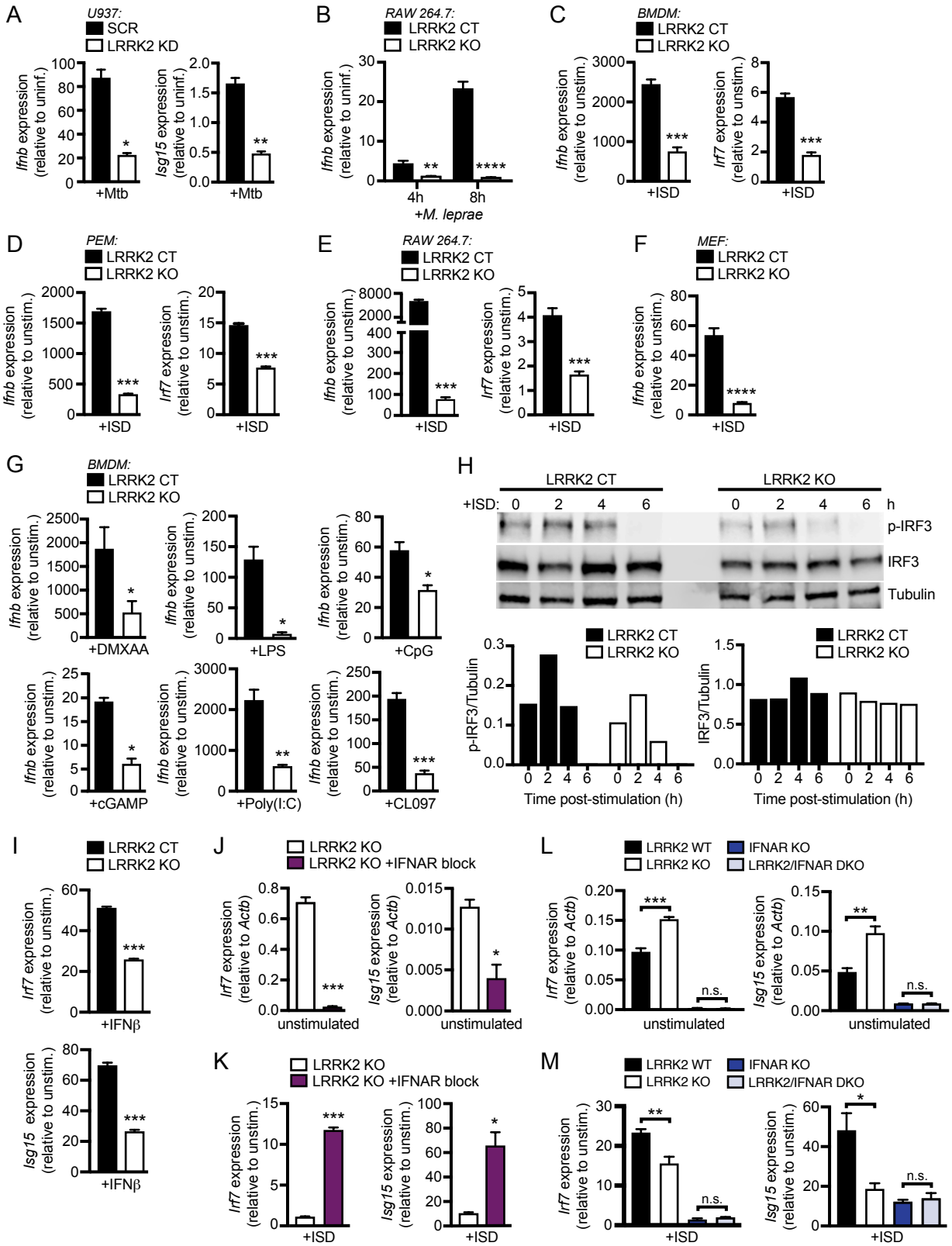

Figure 2. Loss of LRRK2 contributes to type I IFN dysregulation independently of nucleic acid sensing or IFNAR signaling (A) RT-qPCR of Ifnb and Isg15 fold change during Mtb infection in U937 cells with scramble (SCR) or shRNA targeted to Lrrk2 (LRRK2 KD). (B) RT-qPCR of Isg15 fold change at 4 and 8 hours of infection with M. leprae (MOI = 50) in CT or targeted LRRK2 KO RAW 264.7 cells. (C) RT-qPCR of Ifnb and Irf7 fold change following 4hrs transfection with 1μg/ml ISD (dsDNA) in BMDMs from CT or LRRK2 KO mice. (D) RT-qPCR of Ifnb and Irf7 fold change following 4hrs transfection with 1μg/ml ISD in peritoneal macrophages from CT or LRRK2 KO mice elicited for 4 days with 1ml 3% Brewer's thioglycolate broth. (E) As in (D) but in RAW 264.7 CT or LRRK2 KO cells. (F) As in (D) but in MEFs from day 14.5 CT or LRRK2 KO embryos. (G) RT-qPCR of Ifnb gene fold change in LRRK2 CT or KO BMDMs following stimulation with 50ng/ml DMXAA (2hrs), 100ng/ml LPS (4hrs), transfection with 10uM CpG 2395 (4hrs), 1μg/ml cGAMP (4hrs), 1ug/ml poly I:C (dsRNA) (4hrs) or stimulation with 1uM CL097 (4hrs). (H) Western blot of IRF3 phosphorylated at Ser396 (p-IRF3), total IRF3 and tubulin, at 0, 2, 4, 6hrs post transfection with 1μg/ml ISD in LRRK2 CT or KO BMDMs. Lower graphs show normalization of p-IRF3 and IRF3 to tubulin immunoblot bands via densitometry. (I) RT-qPCR of Irf7 and Isg15 gene fold change following at 4hrs following stimulation with 200IU IFN-β. (J) RT-qPCR of Irf7 and Isg15 gene expression normalized to Actb in LRRK2 KO BMDMs in the presence or absence of overnight blocking with IFN-β neutralizing antibody (1:250). (K) As in (J) but with 1μg/ml ISD transfection for 4h. (L) RT-qPCR of Irf7 and Isg15 gene expression normalized to Actb in BMDMs from CT, LRRK2 KO, IFNAR KO, and double KO (LRRK2 KO/IFNAR KO) mice. (M) As in (L) but following transfection with 1μg/ml ISD (4hrs).

also failed to induce type I IFN in *LRRK2* KO BMDMs (Fig. 2G and S2D) and in *LRRK2* KO PEMs (Fig. S2F).

We next tested whether loss of *LRRK2* impacted the ability of cells to respond to other activators of the type I IFN response outside of the cytosolic DNA sensing cascade. To these ends, we treated *LRRK2* KO and control BMDMs with transfected polyI:C (to activate RNA sensing), LPS (to stimulate TRIF/IRF3 downstream of TLR4), and CpG and CL097 (to stimulate nucleic acid sensing via TLR9 and TLR7, respectively). In all cases, we observed a defect in the ability of *LRRK2* KO BMDMs to induce *Ifnb* and ISGs (Fig. 2G). *LRRK2* KO BMDMs were also defective in ISG expression (*Isg15* and *Irf7*) following recombinant bioactive IFN-β treatment (which directly engages with IFNAR) (Fig. 2I). Consistent with our RT-qPCR data, western blot analysis of IRF3 (Ser 395) after ISD transfection showed a significant defect in the ability of *LRRK2* KO macrophages to respond to cytosolic DNA (Fig. 2H). *LRRK2* KO BMDMs were also defective in ISG expression (*Isg15* and *Irf7*) following recombinant bioactive IFN-β treatment (which directly engages with IFNAR) (Fig. 2I). Based on these collective results, we concluded that *LRRK2* KO macrophages are reprogrammed in such a way that they cannot properly induce type I IFN expression regardless of the innate immune stimulus received.

We next hypothesized that the increased basal levels of type I IFN transcripts were driving the inability of *LRRK2* KO macrophages to properly induce a type I IFN response. To test this, CT and *LRRK2* KO BMDMs were treated with an IFN-β neutralizing antibody to prevent engagement of IFNAR and downstream signaling. As predicted, this IFN-β blockade decreased basal transcript levels of *Irf7* and *Isg15* in *LRRK2* KO cells to levels similar to CT cells (Fig. 2J) and remarkably, restored the ability of *LRRK2* KO BMDMs to fully induce type I IFN expression following ISD transfection (Fig. 2K). We further validated that loss of IFNAR signaling rescues the *LRRK2* KO BMDM phenotype by crossing *LRRK2* KO mice to IFNAR KO mice and observed a significant reduction in ISG levels in *LRRK2*/IFNAR double KO BMDMs (Fig. 2L) and upon stimulation normalized their induction of type I IFNs and ISGs to that of controls (Fig 2M). Together, these results indicate that cytosolic nucleic acid and IFNAR signaling pathways are all intact in *LRRK2* KO macrophages, but chronic elevated basal type I IFN expression renders these cells refractory to innate immune stimuli.

Increased basal IFN in *LRRK2* KO macrophages is dependent on cytosolic DNA sensing through cGAS.

Because IFN-β blockade and loss of IFNAR normalized ISG expression in *LRRK2* KO macrophages, we hypothesized that *LRRK2* contributes to basal type I IFN expression

upstream of the cytosolic DNA sensing pathway. To directly test the involvement of cGAS in generating elevated resting levels of type I IFN in *LRRK2* KO macrophages, we crossed *LRRK2* KO and cGAS KO mice and compared type I IFN transcript levels in double KO BMDMs with those of littermate controls. As expected, loss of cGAS led to lower resting *Ifnb* and *Isg15* expression (Schoggins et al., 2014) and knocking out cGAS in a *LRRK2* KO background rescued the elevated basal IFN and ISG expression (Fig. 3A and S3A). With lowered resting type I IFN levels, cGAS/*LRRK2* double KOs were able to respond normally to IFN/ISG-generating innate immune stimuli like LPS or cGAMP and DMXAA (both of which bypass cGAS and stimulate STING directly) (Diner et al., 2013), but not ISD (Fig. 3B and S3A, respectively). Together, these results indicate that the high basal levels of type I IFN in *LRRK2* KO macrophages are due to engagement of the cGAS-dependent DNA sensing pathway.

Cytosolic sensing of mtDNA contributes to basal type I IFN expression in *LRRK2* KO macrophages

We next sought to identify the source of this cGAS-activating signal. Mitochondrial DNA (mtDNA) has been shown to be a potent activator of type I IFN downstream of cGAS (Yang et al., 2014), and *LRRK2* is known to influence mitochondrial homeostasis, albeit through mechanisms that are not entirely clear. To begin to implicate mtDNA in type I IFN dysregulation in *LRRK2* KO macrophages, we first observed the status of the mitochondrial network in MEFs from control and *LRRK2* KO mice. As has previously been described for cells overexpressing *LRRK2* or mutant alleles of *LRRK2* (Yang et al., 2014), *LRRK2* KO MEFs had a more fragmented mitochondrial network, especially around the cell periphery (Fig. 3C). We hypothesized that this fragmentation was a sign of mitochondrial damage and could allow mitochondrial matrix components, including mtDNA, to leak into the cytosol. Therefore, we isolated the cytosolic fraction of control and *LRRK2* KO MEFs and measured cytosolic mtDNA levels. We found that *LRRK2* KO MEFs had ~2-fold higher levels of total mtDNA compared to controls, and importantly, the *LRRK2* KO cells had ~2-fold more cytosolic mtDNA (Fig. 3D-E). To exacerbate the proposed defect, we treated BMDMs with the Bcl2/caspase inhibitors ABT737/OVD-PH, which together induce mitochondrial stress and spillage of mtDNA into the cytosol. As expected, type I IFN and ISG gene expression was induced but was decreased in *LRRK2* KO cells while *Tnf* transcript levels remained unaffected (Fig. 3F and S3B-C). We also sought to exacerbate the *LRRK2* defect by crossing *LRRK2* KO mice with *TFAM* HET mice, which are deficient in the mitochondrial transcription factor required for maintaining the mitochondrial network (Kasashima et al., 2011; West et al., 2015). Double *LRRK2 KO/TFAM*

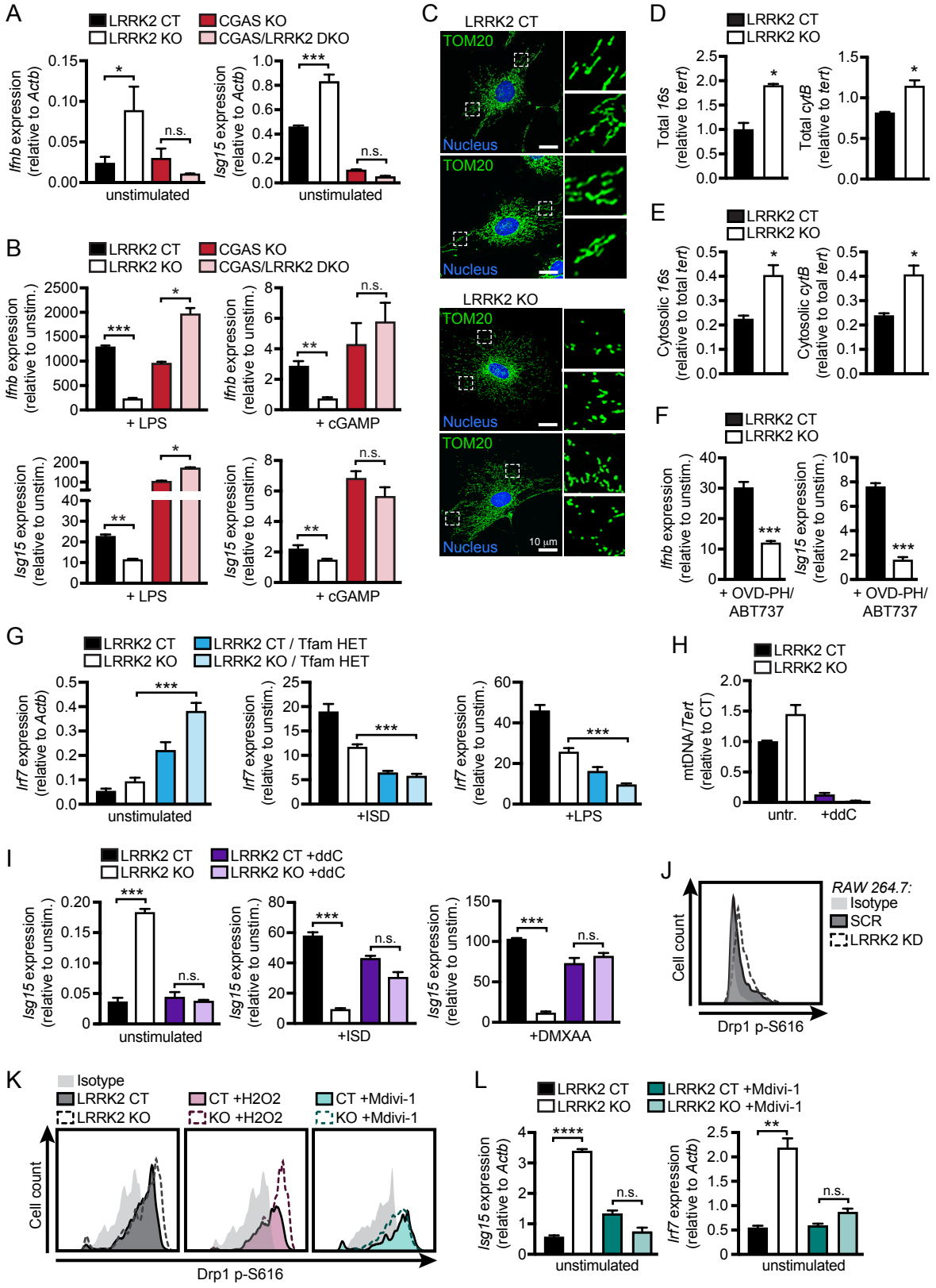

Figure 3. Mitochondrial DNA contributes to type I IFN dysregulation in LRRK2 KO macrophages (A) RT-qPCR of Ifnb and Isg15 gene expression normalized to Actb in BMDMs from CT, LRRK2 KO, cGAS KO, and double KO (LRRK2 KO/cGAS KO) mice. (B) Ifnb and Isg15 gene expression fold change was measured by RT-qPCR in BMDMs following stimulation with 100ng/ml LPS or transfection with 1µg/ml cGAMP for 4hrs. (C) Mitochondrial network of CT and LRRK2 KO MEFs were analyzed by immunofluorescence microscopy. TOMM20 (green) nucleus (blue) (D) qPCR of total 16s and cytB (mitochondrial DNA) relative to Tert (nuclear DNA). (E) As in (D) but cytosolic mitochondrial DNA. (F) Ifnb and Isg15 gene expression fold change was measured by RT-qPCR following 6hr treatment with 10uM ABT737 (BCL2 inhibitor) and 10uM OVD-PH (caspase inhibitor) in CT and LRRK2 KO BMDMs. (G) Irf7 gene expression normalized to Actb in BMDMs from CT, LRRK2 KO, Tfam Het, and double (LRRK2 KO/TFAM HET) mice and Irf7 fold induction following transfection of 1ug/ml ISD (4hr) or 4hr stimulation with 100ng/ml LPS. (H) mtDNA depletion was measured by qPCR dLOOP (mitochondrial) normalized to Tert(nuclear) in CT and LRRK2 KO RAW264.7 cells treated with 10uM ddC for 4 days (I) Isg15 gene expression was measured by RT-qPCR in resting, or 4hrs post 1ug/ml ISD transfection, or DMXAA stimulation in CT and LRRK2 KO RAW264.7 cells with or without ddC treatment. (J) Histogram showing counts of phospho S616-Drp1 in CT and LRRK2 KD RAW 264.7 cells as measured by flow cytometry. (K) As in (J) but for MEFs treated with 100uM H2O2, or with the Drp1 inhibitor Mdivi-1 50uM 12hrs (L)Phospho Drp1 FLOW (K) Basal gene expression of Isg15 and Irf7 in BMDMs treated with or without Mdivi-1 50uM for 12hrs.

Het BMDMs had even further elevated type IFN and ISG gene expression and they were similarly defective at inducing ISGs upon innate immune stimulation (ISD or LPS) (Fig. 3G). Together, these data suggest that spillage of mtDNA into the cytosol in *LRRK2* KO cells contributes to their defective type I IFN expression.

To further implicate mtDNA in contributing to abnormal type I IFN responses in *LRRK2* KO cells, we sought to rescue the defect by depleting mtDNA using ddC, an inhibitor of mtDNA synthesis, or ethidium bromide (EtBr), an intercalating agent shown to deplete mtDNA in dividing cells (Leibowitz, 1971; Meyer and Simpson, 1969). Treating *LRRK2* KO RAW 264.7 cells with ddC or EtBr reduced mtDNA copy number (Fig. 3H-I, S3D, and S3E-F respectively), and normalized IFN and ISG expression in resting *LRRK2* KO cells. Importantly, *LRRK2* KO macrophages depleted of mtDNA showed a restored type I IFN response when stimulated with ISD or treated with DMXAA (Fig. 3I and S3D-F). Collectively, these results demonstrate a critical role for mtDNA in driving both the high basal levels of type I IFN and the inability to properly induce type I IFN expression in *LRRK2* KO macrophages.

Previous studies of microglia have shown that Lrrk2 contributes to mitochondrial homeostasis through interaction with the mitochondrial fission protein Drp1 (Ho et al., 2018). Thus, we hypothesized that the loss of *LRRK2* may compromise mitochondrial stability via misregulation of Drp1 activity and spillage of mtDNA into the cytosol. Looking grossly at Drp1, we observed Drp1+ puncta via immunofluorescence microscopy at the ends of fragmented mitochondria in *LRRK2* KO MEFs, but the total levels and overall distribution did not differ between the CT and KO cells (Fig. S3G). Drp1 fission is positively regulated by its phosphorylation at Ser616 (Taguchi et al., 2007). Therefore, to measure Drp1 activity in control and *LRRK2* KO cells, we performed flow cytometry with an antibody specific for phospho-S616 Drp1. We found increased p616 in resting LRRK2 KD RAW and KO MEFs compared to CT cells (Fig. 3J-K). Next, to test whether Drp1 activity influences ISG expression in *LRRK2* KO cells, we chemically inhibited Drp1 with Mdivi-1 and measured basal gene expression by RT-qPCR. In *LRRK2* KO BMDMs and *LRRK2* KD RAW macrophages, Drp1 inhibition returned ISG expression in *LRRK2* KO cells to control levels (Fig. 3L and S3H). Moreover, Drp1 inhibition also restored the cytosolic mtDNA levels in *LRRK2* KO cells to those of CT cells (Fig. S3I and S3J) This is consistent with an indirect function of Drp1 in mtDNA replication (Parone et al., 2008). Together, these data indicate that aberrant ISG basal expression and induction in *LRRK2* KO cells is caused by leakage of mtDNA into the cytosol, downstream of excessive Drp1-induced mitochondrial fission.

***LRRK2* KO macrophages are susceptible to mitochondrial stress and have altered cellular metabolism.**

Given that cytosolic mtDNA contributes to type I IFN defects in *LRRK2* KO macrophages, we predicted that mitochondria in *LRRK2* KO cells may be more damaged or more prone to damage. To better understand the health of the mitochondrial network in *LRRK2* KO vs. CT macrophages, we first used the carbocyanine dye, JC-1. JC-1 dye accumulates in mitochondria dependent on membrane potential resulting in red fluorescent J-aggregates. Upon loss of membrane potential JC-1 diffuses into the cytosol where it emits a green fluorescence as a monomer. Thus, a reduction in red/green fluorescence intensity signifies mitochondrial depolarization allowing for a sensitive assessment of mitochondrial membrane potential. Flow cytometry analysis of resting CT and *LRRK2* KO cells revealed lower levels of JC-1 dye aggregation (i.e. lowered mitochondrial membrane potential) in *LRRK2* KO BMDMs (Fig. 4A-B), *LRRK2* KD RAW 264.7 macrophages (Fig. S4A), and primary *LRRK2* KO MEFs (Fig. S4B-C), compared to CT cells. In addition, *LRRK2* KO cells were more sensitive to the mitochondrial damaging and depolarizing agents, rotenone and ATP, which is consistent with the *LRRK2* KO cells harboring a baseline mitochondrial defect (BMDMS: Fig. 4C-D, RAW264.7 and MEFs: Fig. S4B-C).

Previous reports have indicated that *LRRK2* dysfunction alters reactive oxygen species (Pereira et al., 2014; Russo et al., 2019). To test whether ROS could contribute to the defective type I IFN signature in *LRRK2* KO cells, we treated control and *LRRK2* KO BMDMs with mitoTEMPO (mitoT), a mitochondrially-targeted scavenger of superoxide (Liang et al., 2010). *LRRK2* KO cells treated with mitoT had normal basal ISG expression levels (Fig. 4E) and induced IFN and ISG to levels comparable to control cells following ISD transfection (Fig. 4F). We also hypothesized that mitochondrial defects may render *LRRK2* KO macrophages incapable of meeting metabolic demands in response to carbon sources. To test this idea, we added sodium pyruvate, an intermediate metabolite of glycolysis and the TCA cycle, to *LRRK2* KO and control RAW 264.7 cell media (DMEM + 10% FBS) and indeed, observed that sodium pyruvate exacerbated high basal levels of type I IFN and decreased induction of ISGs in *LRRK2* KO macrophages in a dose-dependent fashion (Fig. S4D-E).

We next used the Agilent Seahorse Metabolic Analyzer to further investigate the nature of the mitochondrial defect in *LRRK2* KO macrophages. In this assay, oxidative phosphorylation (OXPHOS) and glycolysis are assayed by oxygen consumption rate (OCR) and extracellular acidification rate (ECAR), respectively. We found that OCR in *LRRK2* KO BMDMs was defective both in terms of maximal and reserve capacity (Fig. 4G upper graph), indicating reduced

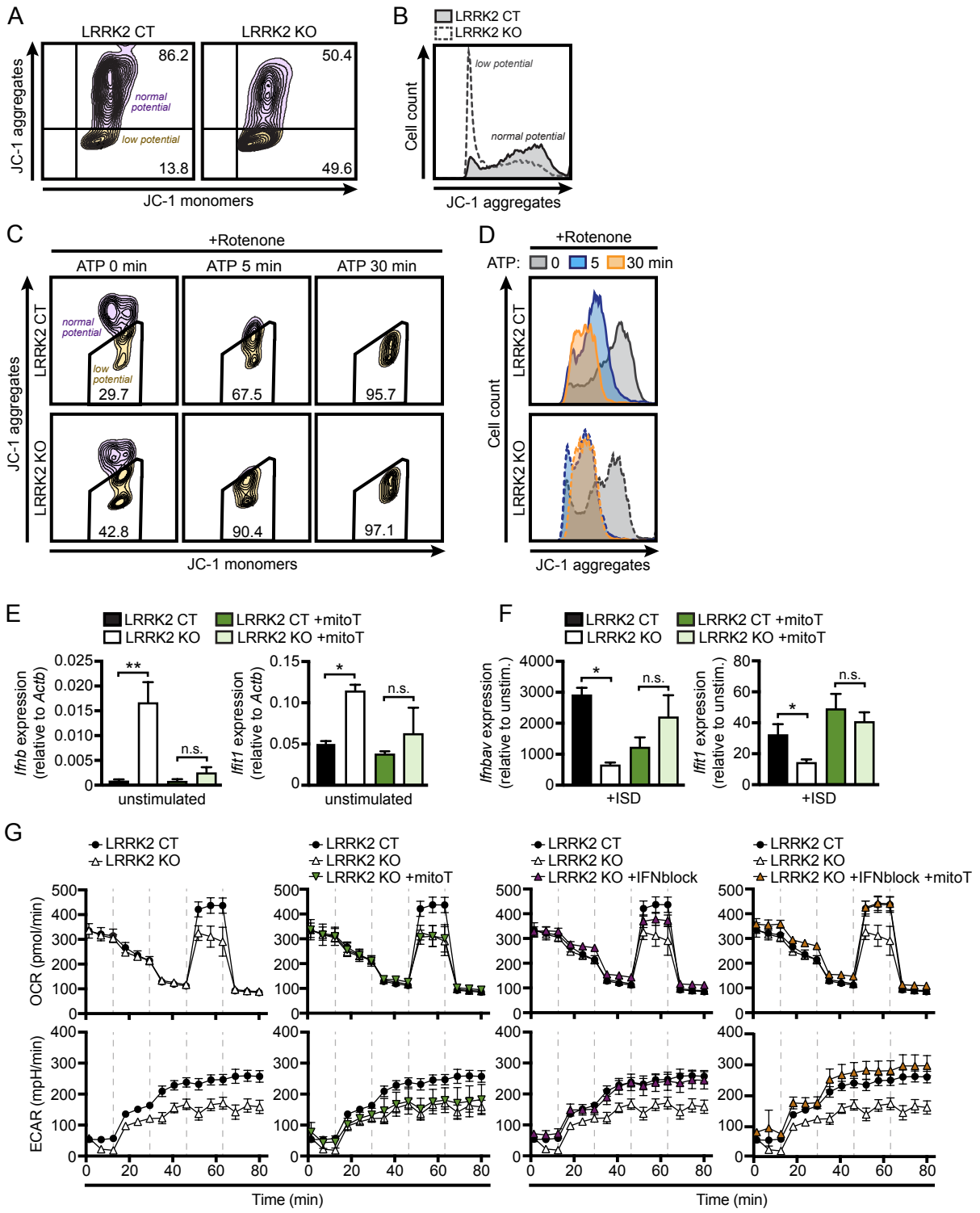

Figure 4. LRRK2 KO macrophages have increased mitochondrial stress and altered metabolism (A) Flow cytometry of LRRK2 CT and KO BMDMs. mitochondrial membrane potential as measured by JC-1 dye aggregates (610/20) normal membrane potential vs monomers (520/50) low membrane potential. (B) Histogram showing cell counts of JC-1 aggregates measured by flow cytometry for LRRK2 CT and KO BMDMs. (C) JC-1 aggregates vs. monomers measured by IF Cytation 5. (D) JC-1 aggregates measured by flow cytometry in BMDMs treated for 3hrs with 2.5μM Rotenone followed by 5μM ATP for the indicated times. (E) Ifnb and Ifit mRNA expression measured by RT-qPCR in LRRK2 CT and KO BMDMs treated overnight with 200μM mitoTEMPO. (F) As in (E) following 4hrs transfection with 1ug/mL ISD. (G) BMDMs from LRRK2 CT and KO mice were treated with 200μM mitoTEMPO, IFN-β blocking antibody, and the combination of both overnight followed by analysis of Oxygen consumption rate (OCR) and extracellular acidification rate (ECAR) measured using the Seahorse Metabolic Analyzer (Agilent).

mitochondrial metabolism. Defects in non-glycolytic acidification, maximal, and reserve capacity were also detected, indicating reduced glycolysis (Fig. 4G lower graph). This result was surprising as cells typically switch from utilizing OXPHOS to glycolysis when activated (Kelly and O'Neill, 2015). Remarkably, co-treatment of *LRRK2* KO BMDMs with mitoT and IFN-β neutralizing antibody completely restored OCAR and ECAR. This rescue was greater than treatment of either IFN-β Ab or mitoT alone (Fig. 4G). We also measured OCR and ECAR in the presence of sodium pyruvate and observed an even greater defect in reserve and maximal capacity in *LRRK2* KO vs. CT macrophages (Fig. S4F). Collectively, these data demonstrate that loss of *LRRK2* in macrophages has profound impact on the mitochondria, whereby loss of mitochondria are less capable of effectively processing high energy electrons produced by the TCA cycle.

Reduced antioxidants and purine biosynthesis metabolites contribute to mitochondrial damage and type I IFN expression in LRRK2 KO macrophages

To better understand possible mechanisms driving, or resulting from, damaged mitochondria in *LRRK2* KO macrophages, we performed an unbiased query of metabolites using LC/MS/MS (Zhou et al., 2012). Looking at metabolites with significant differences, we noted lower levels of IMP and hypoxanthine, intermediates in the purine biosynthesis pathway (Fig. 5C) in *LRRK2* KO cells (Table S2), which we confirmed using pure molecular weight standards (Fig. 5A-C and S5A-B). Interestingly, purine metabolism is tightly associated with generation of antioxidant compounds and several metabolites in this pathway are well-characterized biomarkers of PD (Chen et al., 2012). Consistent with these defects in purine metabolism, we observed significantly fewer puncta containing formylglycinamidine ribonucleotide synthase (FGAMS, also known as PFAS), a core purinosome component, per *LRRK2* KO cell compared to control cells (Fig. 5D-E). Consistent with lower levels of antioxidants, we detected increased oxidized glutathione and glutamate metabolism compounds in *LRRK2* KO macrophages (Table S2).

Because depleted antioxidant pools (and concomitant accumulation of ROS) can lead to mitochondrial damage, we hypothesized they might contribute to the mitochondrial and type I IFN defects we observe in *LRRK2* KO macrophages. To test this, we first supplemented cells with antioxidants directly in order to rescue the type I IFN defect in *LRRK2* KO macrophages. Addition of urate consistently reduced basal ISG levels in *LRRK2* KO BMDMs (Fig 5F), and urate treatment restored the ability of *LRRK2* KO BMDMs to induce type I IFN upon stimulation with LPS or ISD (Fig 5G). In addition, treatment with urate or mitoT restored the resting

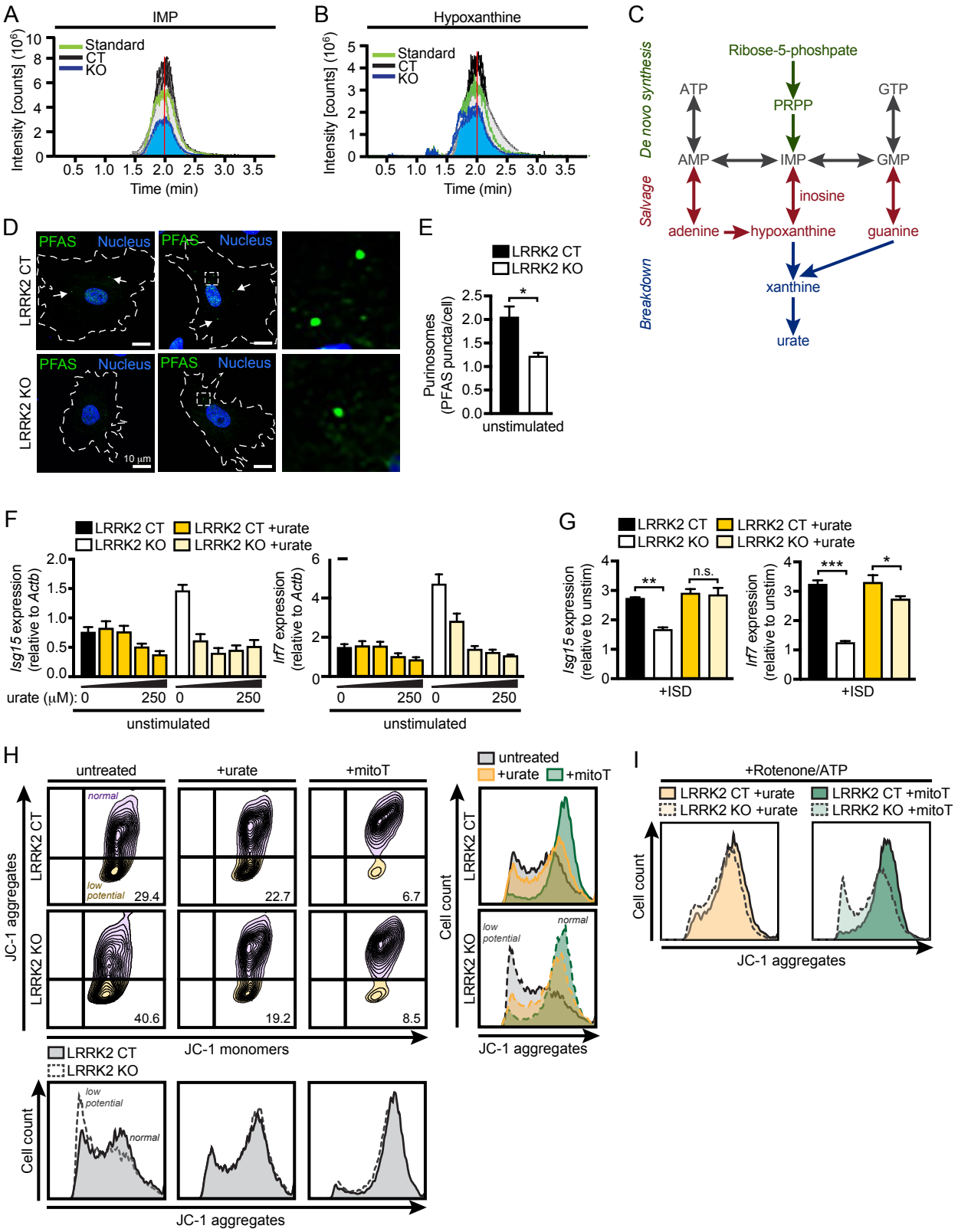

Figure 5. Reduced antioxidant pools in LRRK2 KO macrophages results in mitochondrial stress (A) Chromatogram depicting targeted metabolomic analysis of LRRK2 CT and KO BMDMs with pure molecular weight standard to IMP. (B) the same as (A) but for hypoxanthine (C) Diagram of key metabolites produced during purine metabolism oriented to the major steps of the pathway. De novo synthesis (green), Salvage (red), breakdown (blue). (D) Representative IF of purinosome formation measured by PFAS puncta (green) nuclei (blue) in LRRK2 CT and KO MEFs. (E) Quantification of Pfas puncta per cell. (F) Isg15 and Irf7 gene expression relative to Actb measured by RT-qPCR in BMDMs from LRRK2 CT and KO mice treated with increasing concentrations of urate, 10uM, 50uM, 100uM, 250uM for 24hrs. (G) Isg15 and Irf7 mRNA fold induction measured by RT-qPCR in LRRK2 CT and KO BMDMs treated with or without 100µM urate for 24hrs. (H) JC-1 aggregate vs. monomer formation measured by flow cytometry in BMDMs from LRRK2 CT and KO mice treated with or without urate 100µM, and mitoTEMPO 200µM o/n. (I) Histograms of (H) in the presence of rotenone 3h (2.5µM) followed by ATP 15min (5µM).

mitochondrial membrane potential of *LRRK2* BMDMs (Fig. 5H, histogram in 5I). Collectively, these results suggest that the depletion of antioxidant pools in *LRRK2* KO macrophages downstream of defective purine metabolism contributes to their mitochondrial dysfunction and aberrant type I IFN expression signature.

LRRK2 KO mice control Mtb infection similarly but have altered infection-induced neuroinflammation

Previous reports have linked SNPs in *LRRK2* with susceptibility to mycobacterial infection in humans, and our studies indicate that *LRRK2* plays a key role in homeostasis of macrophages, the first line of defense and replicative niche of Mtb. Therefore, we sought to understand how *LRRK2* deficiency influences innate immune responses *in vivo* during Mtb infection. We infected control and LRRK2 KO mice with ~150 CFUs via aerosol chamber delivery. At 7, 21, 63, and 126 days post-infection, we observed no significant differences in bacterial burdens in the lungs or spleen of infected mice (Fig. S6A). We also measured serum cytokines and tissue cytokine expression and found no major differences (Fig. S6D-E). However, upon inspection of lung tissues via H&E staining, we observed significantly more neutrophils (polymorphonuclear leukocytes, PMNs) in the lungs of *LRRK2* KO mice 21 days post-infection (Fig. 6A-B). Furthermore, the percentage of neutrophils that were necrotic (degenerate PMNs) was higher in the infected *LRRK2* KO mice than in the controls (Fig. 6B). The *LRRK2* KO mice also had more granulomatous nodules, indicating more macrophage-like cells had infiltrated the infected lungs (Fig. S6B-C). Together, these results indicate that while control and LRRK2 KO mice did not display different bacterial burdens, the KO mice had an overly robust innate immune response early during Mtb infection.

Effect of _LRRK2_ and TB infection on microglia reactivity in the dorsal lateral striatum (DLS), substantia nigra pars compacta (SNc), and ventral tegmental area (VTA)

Several lines of evidence point to a connection between persistent infections and neurodegenerative disease and several links between *LRRK2* and neuroinflammation have been previously reported (De Chiara et al., 2012; Schildt et al., 2019). Therefore, we set out to investigate markers of neuroinflammation in the brains of infected mice and uninfected controls. We first focused on microglia since these are the cells of the central nervous system (CNS) that play important roles in neuroimmune surveillance, similar to macrophages in the periphery (Ousman and Kubes, 2012). To assess the extent to which Mtb infection alters microglia reactivity in *LRRK2* CT and KO mice, we focused on three brain structures relevant to PD.

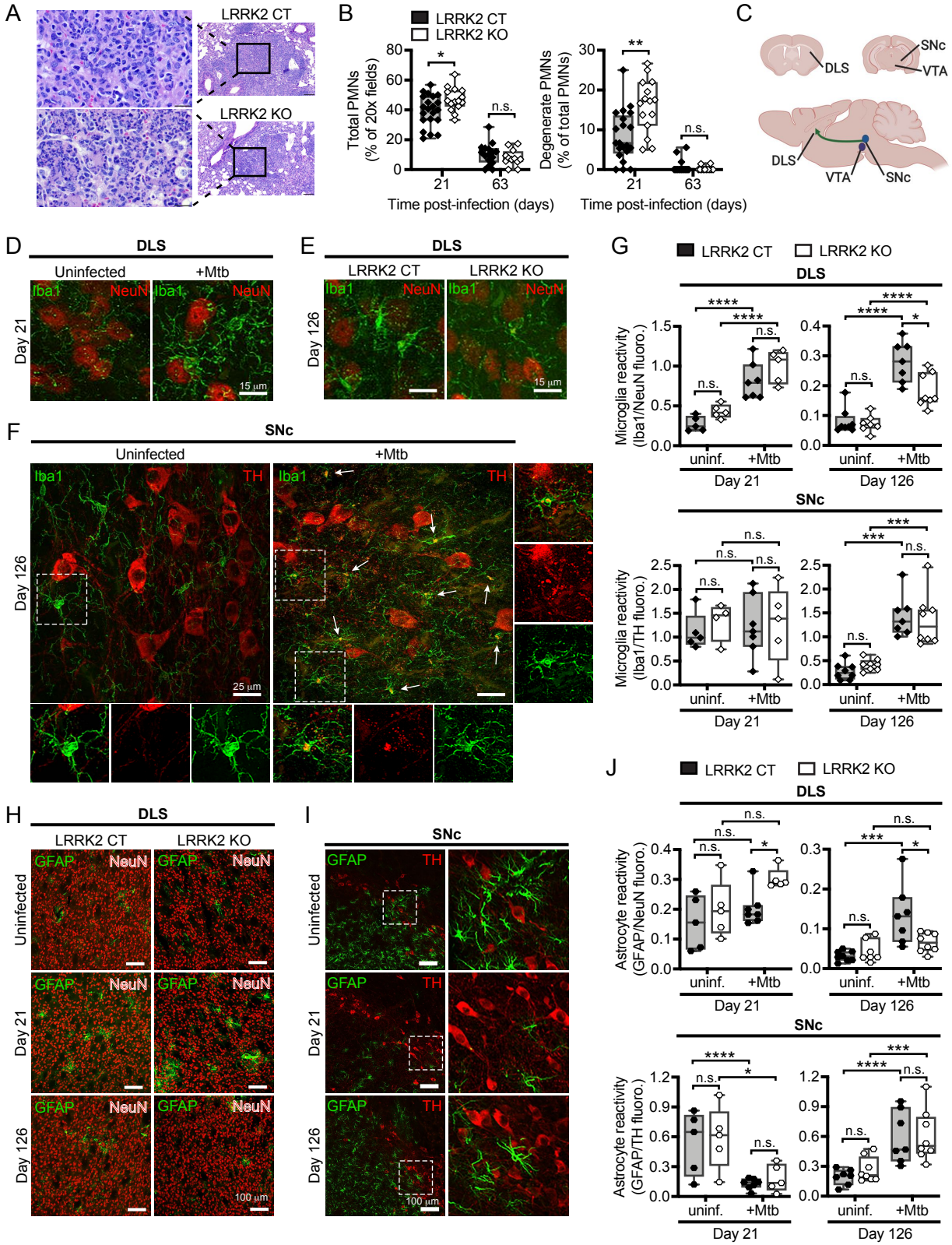

Figure 6. LRRK2 KO mice exhibit increased lung pathology and activation of glial cells in the brain during Mtb infection (A) Histology of an inflammatory nodule in the lungs of LRRK2 KO and CT mice 21 days after infection with Mtb. Hematoxylin and eosin (H&E) stain. (B) Semi-quantification of neutrophils in the lungs of LRRK2 KO and CT mice infected with Mtb for 21 or 63 days. Total neutrophil scores were determined by the percentage of fields of view at 20X magnification containing neutrophils. Degenerate neutrophil scores were determined by the percentage of PMN positive fields containing degenerate neutrophils. (C) Schematic representation of the areas of interest in the nigrostriatal dopaminergic pathway in the mouse brain highlighting the VTA, SNc and DLS. (D) Fluorescence images of the DLS from LRRK2 KO and CT mice uninfected or infected with Mtb for 21 days and immunolabeled with anti-Iba1 and anti-NeuN. Created using BioRender. (E) Fluorescence images of the DLS from LRRK2 KO and CT mice uninfected or infected for 126 days and immunolabeled with anti-Iba1 and anti-NeuN. (F) Fluorescence images of the SNc immunolabeled with anti-TH and anti-Iba1 in uninfected and Mtb-infected (Day 126). (G) Quantification of microglial reactivity in the DLS and SNc from LRRK2 KO and CT mice infected with Mtb for 21 or 126 days and uninfected age matched controls. Microglia reactivity was determined by Iba1 immunofluorescence normalized to NeuN or TH immunofluorescence in the DLS and SNc respectively. (H) Fluorescence images of the DLS from LRRK2 KO and CT mice immunolabeled with GFAP and NeuN in LRRK2 KO and CT mice infected with Mtb for 21 or 126 days and uninfected age matched controls. (I) Fluorescence images of the SNc from LRRK2 KO and CT mice infected for 21 or 126 days and immunolabeled with GFAP and TH. (J) Quantification of astrocyte reactivity in the DLS and SNc of LRRK2 KO and CT mice infected with Mtb for 21 or 126 days and uninfected age matched controls. Astrocyte reactivity was determined by GFAP immunofluorescence normalized to NeuN or TH immunofluorescence in the DLS and SNc respectively.

These are the dorsolateral striatum (DLS) which contains dopaminergic (DA) terminals, the substantia nigra pars compacta (SNc) and the ventral tegmental area (VTA), both of which contain DA cell bodies (Fig. 6C). Microglia reactivity in the DLS, SNc and VTA was assessed by measuring endogenous Iba1 fluorescence intensity in microglia and normalizing these values to NeuN fluorescence in the DLS or TH fluorescence in the SNc and VTA.

First, we examined the effect of systemic Mtb infection on *LRRK2* CT mice. It is important to note that at all time points examined, there is no evidence of Mtb bacilli in the brains, as measured by acid-fast staining (Fig. S6J). Compared to uninfected mice, infected *LRRK2* CT mice showed significant increases in normalized Iba1 fluorescence in the DLS at 21 and 126 days post-infection (3-fold at day 21) (Fig. 6D & 6F). In contrast, Iba1 fluorescence in the two midbrain structures, SNc and VTA, remained unaltered relative to age-matched uninfected *LRRK2* CT mice at 21 days post-infection, but significantly increased at 126 days post-infection (5-fold in SNc; 2-fold in VTA) (Fig. 6F and S6G).

We next examined microglia reactivity in the DLS, SNc and VTA of *LRRK2* KO mice following systemic Mtb infection. We found that Mtb-infected *LRRK2* KO mice showed a pattern of microglia reactivity in the DLS that was similar to *LRRK2* CT mice. Relative to uninfected *LRRK2* KO mice, we observed a 2-fold increase in Iba1 fluorescence within the DLS at day 21 ($p<0.001$) and a 2.5-fold increase at day 126 ($p<0.001$) post Mtb-infection (Fig. 6F). Compared to age-matched uninfected *LRRK2* KO control mice, Iba1 fluorescence in the SNc and VTA from Mtb infected *LRRK2* KO mice was unchanged at 21 days post-infection ($p=0.89$, SNc; $p=0.33$, VTA), but increased by 3-fold in the SNc ($p<0.001$) and VTA ($p=0.03$) at 126 days post-infection (Fig. 6F and Fig. S6G). Together these data show for the first time that microglia in the three PD-relevant brain regions, the DLS, SNc, and VTA, become reactive following chronic systemic infection with Mtb. Intriguingly, upon close inspection, we observed a high degree of co-localization between Iba1 and TH staining in the Mtb-infected SNc (Day 126) (indicated by arrows in Fig. 6F) and accumulation of TH-positive cellular debris. We speculate that these events correspond to phagocytosis of damaged neurons or neuronal debris, which selectively occurs in the SNc of Mtb-infected mice.

Furthermore, midbrain microglia become reactive at later time points post-Mtb infection than microglia in the DLS with no additional effect of *LRRK2* KO on the pattern or extent of reactivity. In addition, we did not observe any baseline differences in the reactivity profile of microglia across all brain regions or time points between uninfected *LRRK2* KO and *LRRK2* CT mice. The sole exception was a small but significant 1.5-fold decrease in Iba1 in the DLS of *LRRK2* KO compared to CT mice at 126 days-post infection ($p=0.01$) (Fig. 6E-F).

Since the mice were aged for an additional 126 days in our experiments with or without Mtb infection and because aging can alter the expression of Iba1 in microglia, we examined the effect of age on baseline expression of Iba1 in *LRRK2* CT and KO mice. Both groups of mice showed a significant age-dependent reduction in microglia reactivity in the DLS, SNc and VTA when comparing 3.5 month old to 6.5 month old uninfected *LRRK2* CT and KO mice (Fig. S6I) ($p<0.001$ for DLS and SNc; $p=0.016$ for VTA; ANOVA). Mtb infection failed to reduce microglia reactivity in the SNc and VTA from day 21 to 126, while preserving the natural decline of microglia reactivity in the DLS (Fig. 6K and S6J).

Effect of *LRRK2* and Mtb infection on astrocyte reactivity in the dorsal lateral striatum (DLS), substantia nigra pars compacta (SNc), and ventral tegmental area (VTA)

We also assessed the extent to which Mtb infection alters astrocyte reactivity in *LRRK2* CT and KO mice in the DLS, SNc and VTA. Although once considered supporting cells in the CNS, emerging evidence suggests that astrocytes play vital roles in modulating neural circuit activity during physiological and pathological states (Khakh and Sofroniew, 2015). Since GFAP expression levels are known to increase in reactive astrocytes, we measured GFAP fluorescence and normalized values to NeuN fluorescence in the DLS and TH fluorescence in SNc and VTA.

We found that at 21 days post-infection, GFAP levels in *LRRK2* CT astrocytes in the DLS were similar to uninfected mice, but significantly increased after 126 days post Mtb-infection ($p=0.52$ at day 21; 4-fold at day 126, $p=0.002$) (Fig. 6J and I), suggesting that chronic systemic TB infection increases astrocyte reactivity in the DLS. In contrast to the DLS, the SNc showed a more complex profile of astrocyte reactivity. When compared to age-matched uninfected CT mice, SNc astrocytes showed 4-fold lower GFAP fluorescence at day 21 post-infection ($p<0.001$), which increased by 3-fold 126 days post-infection ($p=0.005$) (Fig. 6J). The astrocyte reactivity profile within the VTA of *LRRK2* CT mice was similar to the SNc, but differences at both time points were not significant ($p=0.41$ at day 21; $p=0.10$ at day 126) (Fig. S6H).

Having found large differences in astrocyte reactivity with systemic Mtb infection in *LRRK2* CT mice, we assessed the extent to which astrocytes in *LRRK2* KO mice with systemic Mtb infection showed reactivity in DLS, SNc and VTA. In contrast to *LRRK2* CT mice, Mtb infected *LRRK2* KO mice displayed no significant GFAP differences in the DLS at either time point when compared to uninfected *LRRK2* KO mice ($p=0.10$ at day 21; $p=0.13$ at day 126) (Fig. 6J and I). In addition, we observed that *LRRK2* KO mice followed a pattern of astrocyte

reactivity in the SNc and VTA that was similar to that seen in *LRRK2* CT mice. Astrocytes in the SNc showed significantly lower GFAP at day 21 post-infection, but had significantly higher levels than uninfected *LRRK2* KO mice by day 126 post-infection (3-fold at day 21, p=0.03; 2-fold at day 126, p=0.009) (Fig. 6J). GFAP fluorescence in the VTA were similar at both time points when compared to uninfected mice (p=0.31 at day 21; p=0.08 at day 126) (Fig. S6H). Together these data suggest that astrocytes in CT mice become reactive in the DLS and at later stages of infection, in the SNc following Mtb infection. This pathology mirrors the progression of neurodegeneration in idiopathic PD(Stephens et al., 2005; Villalba et al., 2009; Zaja-Milatovic et al., 2005). In addition, the reactivity of DLS astrocytes following Mtb infection is dependent on *LRRK2* expression, while SNc astrocytes do not depend on *LRRK2* for induction of reactivity following Mtb infection.

We also found an effect of age on astrocyte reactivity in the DLS and SNc. Astrocyte reactivity in uninfected mice showed a significant age-dependent reduction in the DLS and SNc of mice such that old mice showed significantly lower GFAP fluorescence than young mice (p<0.001 for DLS; p=0.023 for SNc; ANOVA) (Fig. S6I). This age-dependent reduction was maintained in the DLS of TB infected mice from day 21 to 126. We observed that Mtb infection caused a loss of age-dependent GFAP reduction in the SNc and VTA (Fig. 6K and S6J). Together these data suggest that systemic TB infection dramatically alters the reactivity profile of astrocytes in the DLS, SNc and VTA and that astrocyte reactivity following Mtb infection is dependent on the expression of *LRRK2*.

Loss of *LRRK2* impacts the capacity of astrocytes to respond to stimuli ex vivo

Because we observed dynamic changes to astrocyte reactivity and microglial activation during the course of Mtb infection *in vivo* we wanted to better understand the response of these cells *ex vivo*, especially in terms of the mitochondrial and type I IFN phenotypes we uncovered in *LRRK2* KO peripheral macrophages. To this end, we differentiated primary cell cultures enriched in astrocytes and microglia from the brains of neonatal CT and *LRRK2* KO mice. As expected, astrocyte cultures were positive for *Gfap* mRNA whereas microglial cultures expressed *Iba1* (Fig. 7A), confirming successful enrichment. *LRRK2* KO astrocyte cultures expressed a mild increase in *Gfap* and *Ccl5* mRNA over CT *ex vivo* (Fig. 7B), indicating an increased reactivity at rest. Remarkably, when stimulated with IFN-β directly or the supernatants of CT macrophages infected with Mtb, *LRRK2* KO astrocyte cultures selectively failed to upregulate these same markers to the extent of CT astrocytes (Fig. 7C, S7A). As we observed in *LRRK2* KO BMDMs, *LRRK2* KO astrocytes also expressed increased ISGs at rest, failed to

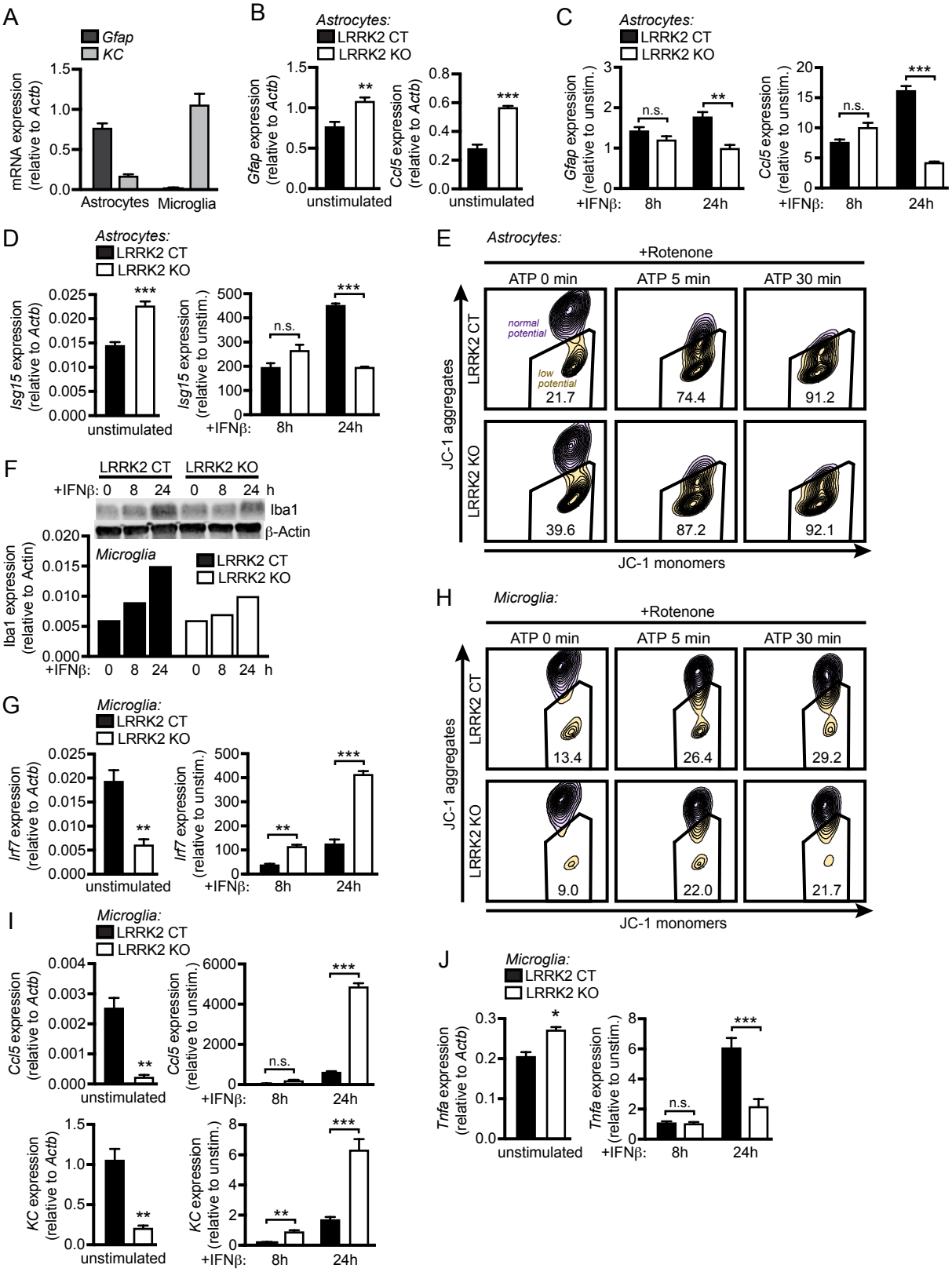

Figure 7. Loss of Lrrk2 alters glial cell activation and reactivity *ex vivo* (A) Gfap, and Iba1 gene expression relative to Actb in astrocyte and microglia enriched primary cell cultures from the brains of P0.5 mice. (B) Gfap and Ccl5 gene expression relative to Actb measured by RT-qPCR in astrocyte cultures. (C) As in (B) but fold induction following stimulation with 800IU IFN-β for the indicated times. (D) qRT PCR of Isg15 gene expression normalized to Actb, and fold induction following stimulation with IFN-β (800IU). (E) JC-1 Dye aggregation measured by flow cytometry in LRRK2 CT and KO astrocyte cultures treated with roteneone 2.5μM followed by 5μM ATP for the indicated time. (F) Immunoblot analysis of Iba1 protein levels in astrocyte cultures with 800IU IFN-β. Bar graph shows protein levels relative to Actb. (G) RT-qPCR of Irf7 gene expression normalized to Actb, and fold induction following stimulation with IFN-β (800IU). (H) JC-1 Dye aggregation measured by flow cytometry in LRRK2 CT and KO microglial cultures treated with roteneone 2.5μM followed by 5 μM ATP for the indicated time. (I) qRT-qPCR of Ccl5 and Kc and fold induction following stimulation with IFN-β (800IU). (J) RT-qPCR of Tnf gene expression normalized to Actb, and fold induction following stimulation with IFN-β (800IU).

robustly upregulate these genes upon stimulation (Fig. 7D), and were sensitive to mitochondrial depolarizing agents relative to CT astrocytes (Fig 7E). Taken together, these results strongly suggest that *LRRK2* KO astrocytes are defective in many of the same ways we observed for peripheral macrophages and begin to elucidate how peripheral infection, coupled with genetic defects, may precipitate neuroinflammation.

We also examined *LRRK2* KO microglia *ex vivo*. *LRRK2* KO microglia exhibited a modest reduction of Iba1 protein levels, compared to CT, upon stimulation with IFN-β (Fig. 7G), consistent with *in vivo* results at D126 post-Mtb infection (Fig. 6F). Surprisingly, *LRRK2* KO microglia had a reduced type I IFN signature at rest and dramatically upregulated ISGs upon stimulation (Fig. 7G). Consistent with this phenotype, *LRRK2* KO microglia were not sensitive to depolarizing stressors (Fig. 7H). *LRRK2* KO microglia also significantly upregulated proinflammatory chemokines *Ccl5* and *KC* over time (Fig. 7I), but failed to upregulate *Tnf* to the extent of *LRRK2* CT microglia (Fig. 7J), indicting that LRRK2 KO microglia may have an alternative proinflammatory polarization compared to CT cells. Together, these data suggest that *LRRK2* KO microglia and astrocytes have altered ability to sense and respond to innate immune cues.

DISCUSSION

Despite being repeatedly associated with susceptibility to mycobacterial infection and other inflammatory disorders in GWAS studies, very little is known about how Lrrk2, a massive, multifunctional protein, functions outside of the central nervous system. Here, we provide evidence that loss of *LRRK2* influences the ability of immune cells—both in the periphery and in PD relevant regions of the brain—to respond to and express inflammatory molecules. During Mtb infection, in peripheral organs like the lungs, these defects manifest themselves at the level of local neutrophil/macrophage infiltration and necrosis without significantly impacting bacterial replication. In the brains of Mtb-infected mice, loss of *LRRK2* sensitizes glial cells like astrocytes and microglia, inducing a hyper-reactive phenotype even when these cells are exposed to the same circulating cytokine milieu as CT mice. Together, these results argue strongly for the "multiple-hit hypothesis" of neurodegenerative disease, whereby genetic susceptibility (e.g. loss of *LRRK2*) coupled with environmental stressors (e.g. Mtb infection (Shen et al., 2016), mitochondrial stress (Tanner et al., 2011), exhaustive exercise (Sliter et al., 2018)) can trigger neuroinflammation and potentially cause downstream damage to neurons (Balin and Appelt, 2001; Patrick et al., 2019).

We propose that dysregulation of type I IFN expression in *LRRK2* KO macrophages is the consequence of two distinct cellular defects conferred by loss of Lrrk2. First, in the absence of Lrrk2, decreased levels of purine metabolites and urate contribute to oxidative stress, leading to damage of the mitochondrial network. A recent human kinome screen identified Lrrk2 as a kinase involved in dynamics of the purinosome, a cellular body composed of purine biosynthetic enzymes that assembles at or on the mitochondrial network (French et al., 2016). Specifically, shRNA knockdown of Lrrk2 in HeLa cells inhibited purinosome assembly and disassembly. As purinosomes are posited to form in order to protect unstable intermediates and increase metabolic flux through the *de novo* purine biosynthetic pathway (An et al., 2008; Schendel et al., 1988; Zhao et al., 2013), we propose that Lrrk2-dependent defects in purinosome assembly lead to lower levels of IMP and hypoxanthine. Lower levels of these purine nucleotide intermediates in *LRRK2* KO macrophages are especially notable in the context of PD, as the plasma of patients (both Lrrk2 mutant and idiopathic) has been shown to contain significantly less hypoxanthine and uric acid levels (uric acid/urate being the final product of the purine biosynthetic/salvage pathway (Fig. 5C) (Johansen et al., 2009) and Lrrk2 mutation carriers with higher urate plasma levels are less likely to develop PD (Bakshi et al., 2019). Indeed, urate is currently being investigated as a potential therapeutic of PD, highlighting the importance of purine biosynthesis in maintaining healthy neurons.

Second, we propose that loss of *LRRK2* contributes to type I IFN dysregulation through phosphorylation of the mitochondria-associated fission protein Drp1. Previous reports have shown that Lrrk2 can physically interact with Drp1 and that Lrrk2 mediates mitochondrial fragmentation through Drp1 (Bakshi et al., 2019). Overexpression of both wild type Lrrk2 and the G2019S allele have been shown to cause mitochondrial fragmentation (X. Wang et al., 2012). Curiously, we observe a similar phenotype in macrophages lacking *LRRK2* (Fig. 3C), suggesting that the balance of Lrrk2 protein levels is crucial for maintenance of the mitochondrial network. Treatment of a microglia cell line (BV2) with the TLR4 agonist LPS has previously been shown to enhance mitochondrial fission and neuroinflammation, which Ho et al. propose occurs by increasing Lrrk2 and DRP1 levels (Ho et al., 2019; Perez-Carrion et al., 2018; Su and Qi, 2013; X. Wang et al., 2012). These results, coupled with our own observations that the Mtb-induced peripheral cytokine milieu can activate microglia and astrocytes, begin to paint a complex picture whereby tipping the balance of Lrrk2 and Drp1 levels in any number of ways can trigger a pathogenic feedback loop, leading to fragmentation of mitochondria and activation of type I IFN responses. In the absence of Lrrk2, lower antioxidant levels (via

aforementioned purinosome abnormalities) likely exacerbate this defect, leading to higher oxidative stress and additional damage to the mitochondrial network.

Although we observed a striking type I IFN defect (both higher basal levels and an inability to induce ISG expression downstream of cytosolic nucleic acid sensing and/or engagement of IFNAR) in a number of primary cells and cell lines, we did not measure a major difference in IFN-β expression, either in circulating serum or in select tissues, at select key time points during Mtb infection. These results were surprising to us, as Mtb is a potent activator of cytosolic DNA sensing (Manzanillo et al., 2012; Watson et al., 2015) and type I IFN is an important biomarker of Mtb infection associated with poor outcomes (Berry et al., 2010). We previously observed an apparent disconnect between type I IFN expression defects in Mtb-infected macrophages and Mtb-infected mice, as loss of the cytosolic DNA sensor cGAS almost completely abrogates type I IFN expression in macrophages but only has minor effects in the serum and lungs in whole KO mice (Watson et al., 2015), suggesting that mechanisms exist *in vivo* to overcome even major defects in nucleic acid sensing and downstream type I IFN expression. Importantly, consistent with our macrophage data, another recent publication that investigated the role of *LRRK2* in controlling *Mtb* infection reported a significant decrease in IFN-α in the lungs of *LRRK2* KO infected animals at Day 56 post-infection (Härtlova et al., 2018).

Because our wild type and *LRRK2* KO mice were able to control *Mtb* replication to similar levels (no significant differences in CFUs), the changes we observe in the brains of these mice cannot be attributed to bacterial loads. Nor can they be readily attributed to differences in circulating cytokines, although it is possible that cytokine levels are significantly different at time points other than those that we measured (as is the reported in Hartlova et al.). Therefore, it is rather remarkable that we observed an increase in microglial reactivity in Mtb infected CT and *LRRK2* KO mice in the DLS, a region that is implicated in the initiation of PD (Villalba et al., 2009). Our data also suggest that reactive microglia are intimately associated with TH+ neuronal debris in the SNc of Mtb-infected mice (Fig. 6F). It is possible that the microglia are phagocytosing pieces of damaged neurons or perhaps damaging the neurons themselves. In either case, the fact that this behavior is only apparent in the brains of Mtb-infected mice strongly suggests that peripheral infection alters interactions between microglia and neurons in potentially pathological ways. It is tempting to speculate that this increase in reactive microglia serves as a mechanism by which persistent infections can precipitate neurodegeneration (Patrick et al., 2019).

In contrast, astrocytes in the DLS become reactive with Mtb infection only in CT mice and not *LRRK2* KO mice. This suggests that astrocytes in the DLS depend on *LRRK2* to initiate reactivity, while microglia do not require *LRRK2* to respond to Mtb infection. Indeed, *LRRK2* mRNA expression in astrocytes in mice is ~6 fold higher than microglia (Y. Zhang et al., 2014). We observed that Mtb infection increases microglial and astrocytic reactivity at later time points (126 days) in the SNc when compared to the DLS. Taken together with our data that KO of *LRRK2* in macrophages and MEFs increases fragmentation of peripheral mitochondria, the differential profile of reactivity in astrocytes between DLS and SNc strongly suggest that astrocytic mitochondria in the SNc are more resilient and likely functionally different from astrocytic mitochondria in the DLS.

These data are the first to directly connect *LRRK2*'s role in maintaining mitochondrial homeostasis to its emerging role in inflammation, both in the brain and in the periphery. Given the striking phenotypes we observed in the brains of Mtb-infected *LRRK2* KO mice, it is tempting to speculate that *LRRK2*s contribution of neuroinflammation and glial cell activation is a major driver of PD, thus opening the door for novel immune-targeted therapeutic interventions designed to halt or slow neurodegenerative disease progression.

ACKNOWLEDGEMENTS

We would like to thank Cory Klemashevich at the TAMU Integrated Metabolomics Analysis Core for his help with the metabolomics analysis. We would also like the acknowledge Monica Britton at the University of California, Davis DNA Technologies & Expression Analysis Core Library for her help with the RNA-seq analysis. We would like to thank A. Phillip West and the West lab for giving suggestions in experimental design regarding mitochondria and for providing us with Tfam Het and cGAS ko mice. We'd lastly like to thank Nevan Krogan at University of California, San Francisco for his help with the conceptual design of this manuscript and other members of the Patrick and Watson labs for discussions and feedback.

METHODS

Mice

LRRK2 KO mice (C57BL/6-Lrrk2$^{tm1.1Mjff}$/J) stock #016121, and IFNAR KO mice (B6(Cg)-Ifnar1$^{tm1.2Ees}$/J) stock #028288 were purchased from The Jackson Laboratories (Bar Harbor, ME). Tfam Het (Woo DK 2012), and cGAS KO (B6(C)-Cgastm1d(EUCOMM)Hmgu/J) mice were provided by A. Phillip West, Texas A &M Health Science Center (Bryan, TX). All mice used in

experiments were compared to age and sex matched controls. In order to ensure littermate controls were used in all experiments *LRRK2* KO crosses were made with (Het) Lrrk2$^{-/-}$ x (KO) Lrrk2$^{+/-}$ mice. Mice used to generate BMDMs and PEMs were between 8-12 weeks old. Mice were infected with Mtb at 10 weeks. Mice used to make glial cultures were P0.5 days old. Embryos used to make primary MEFs were at 14.5 days post coitum. All animals were housed, bred and studied at Texas A&M Health Science Center under approved IACUC guidelines.

M. tuberculosis infections

The Erdman strain was used for all *M. tuberculosis* infections. Low passage lab stocks were thawed for each experiment to ensure virulence was preserved. *M. tuberculosis* was cultured in roller bottles at 37°C in Middlebrook 7H9 broth (BD Bioscienes) supplemented with 10% OADC, 0.5% glycerol, and 0.1% Tween-80 or on 7H11 plates (Hardy Diagnostics). All work with *M. tuberculosis* was performed under Biosafety level 3 containment using procedures approved by the Texas A&M University Institutional Biosafety Committee.

Prior to infection, BMDMs were seeded at $1.2x10^6$ cells/well (6-well dish) or $3x10^5$ cells/well (12-well dish), RAW cells at $5x10^5$ cells/well (12-well dish), and U937s at $1x10^6$ cells/well. U937s were cultured with 10ng/ml phorbol 12-myristate 13-acetate (PMA) for 48 hr to induce differentiation and then recovered in fresh media for an addition 24 hr prior to infection.

To prepare the inoculum, bacteria grown to log phase (OD 0.6-0.8) were spun at low speed (500g) to remove clumps, and then pelleted and washed with PBS twice. Resuspended bacteria were briefly sonicated and spun at low speed once again to further remove clumps. The bacteria were diluted in DMEM + 10% horse serum and added to cells at an MOI of 10. Cells were spun with bacteria for 10 min at 1000g to synchronize infection, washed twice with PBS and then incubated in fresh media. RNA was harvested from infected cells using 0.5-1ml Trizol reagent 4h post-infection unless otherwise indicated.

Mouse infections

All infections were performed using procedures approved by Texas A&M University Institutional Care and Use Committee. The *M. tuberculosis* inoculum was prepared as described above. Age- and sex-matched (approximately 3-month-old male and female littermates) were infected via inhalation exposure using a Madison chamber (Glas-Col) calibrated to introduce 100-200 CFUs per mouse. For each infection, approximately 5 mice were euthanized immediately, and

their lungs were homogenized and plated to verify an accurate inoculum. Infected mice were housed under BSL3 containment and monitored daily by lab members and veterinary staff.

At the indicated time points, mice were euthanized, and tissue samples were collected. Organs were divided in order to maximize infection readouts (CFUs: left lobe lung and ½ spleen; histology: 2 right lung lobes and ¼ spleen; RNA: 1 right lung lobe and ¼ spleen). For histological analysis organs were fixed for 24 hr in neutral buffered formalin and moved to ethanol (lung, spleen) or 4% paraformaldehyde and moved to 30% sucrose (brain). Organs were further processed as described below. For cytokine transcript analysis, organs were homogenized in Trizol, and RNA was isolated as described above. For CFU enumeration, organs were homogenized in 5 ml PBS + 0.1% Tween-80, and serial dilutions were plated on 7H11 plates. Colonies were counted after plates were incubated at 37° for 3 weeks. Blood was collected in serum collection tubes, allowed to clot for 1-2 hr at room temperature, and spun to separate serum. Serum cytokine analysis was performed by Eve Technologies.

Histopathology

Lungs and spleens were fixed with paraformaldehyde, subjected to routine processing, embedded in paraffin, and 5-µm sections were cut and stained with hematoxylin and eosin (H&E) or acid-fast stain (Diagnostic BioSystems). A boarded veterinary pathologist performed a masked evaluation of lung sections for inflammation using a scoring system: score 0, none; score 1, up to 25% of fields; score 2, 26-50% of fields; score 3, 51-75% of fields; score 4, 76-100% of fields. To quantify the percentage of lung fields occupied by inflammatory nodules, scanned images of at least 2 sections of each lung were analyzed using Fiji Image J (Schindelin et al., 2012) to determine the total cross-sectional area of inflammatory nodules per total lung cross sectional area. For acid fast staining, one brain hemisphere was fixed with paraformaldehyde for 48 hours, then transferred to a cryoprotective buffer (30% sucrose in a phosphate buffer), and frozen for coronal slicing into 40-µm sections. At least two sections per mouse were stained with an acid-fast stain (Diagnostic BioSystems) according to the manufacturer's instructions and visualized by an Olympus BH2 light microscope.

Tissue Immunohistochemistry

Immunohistochemistry was performed on uninfected C57/BL6NJ mice and mice that were infected with mycobacterium tuberculosis (TB). Two genotypes of mice were utilized for these experiments: heterozygous LRRK2$^{+/-}$ (Het) or knockout LRRK2$^{-/-}$ (KO). Brains from Het

(CT) and KO mice were collected on days 7, 21, or 126 after initiation of tuberculosis infection. To specifically evaluate the effect of TB on astrocytes and microglia, we collected brains from sham infected Het and KO mice 21 and 126 days after sham infection.

Striatal and midbrain sections from these mice were stained for glial fibrillary acid protein (GFAP) to label astrocytes, Iba-1 to label microglia, and NeuN for neurons in striatal slices. In addition to Iba1 and GFAP, tyrosine hydroxylase (TH) labeling was used for visualizing dopaminergic neurons in the midbrain.

For immunohistochemistry, mice were anesthetized with isoflurane and quickly decapitated. The brain was gently removed from the skull and postfixed in 4% paraformaldehyde overnight at 4°C. The tissue was cryoprotected in 30% sucrose + PBS solution for 48-72 hours. 40 μm thick coronal sections were obtained using a cryostat microtome (Leica) and preserved in 0.01% sodium azide + PBS at 4°C.

Immunohistochemistry was performed using previously published techniques (Srinivasan et al., 2015; 2016). Briefly, sections were washed 3x for 10 min in 1X TBS, then blocked for 1 hr in 5% NGS and 0.25% Triton-X-100 in 1X TBS at RT. Sections were incubated overnight at 4°C in primary antibodies diluted in blocking solution. The following primary antibodies were used: rabbit anti-GFAP (1:1000; Abcam ab7260), rabbit anti-Iba1 (1:250; Wako Chemical 019-19741), mouse anti-NeuN (1:500; Abcam ab104224), and chicken anti-TH (1:1000; Abcam ab76442). The following day sections were washed 3x for 10 min each in 1X TBS and incubated with appropriate secondary antibodies in blocking solution for 2 hr at RT. The following secondary antibodies were used: goat anti-rabbit (1:1000; Abcam ab150077), goat anti-mouse (1:1000; Abcam ab150120), and goat anti-chicken (1:1000; Abcam ab150176). The sections were rinsed 3x for 10 min in 1X TBS and then mounted on microscope slides in Fluoromount (Diagnostic Biosystems; K024) and coversliped for imaging.

Tissue Imaging

Images were obtained using a FV 1200 Olympus inverted confocal microscope equipped with 20x, 0.85 NA oil immersion objective, 473 nm, and 561 nm laser lines to excite appropriate Alexa Fluor secondary antibodies. Images were obtained at 1x digital zoom. HV, gain, and offset was adjusted so that fluorescent signals from images were just below saturation. Laser power for 473 and 561 excitation lines were maintained between 2-3% of maximum. All images were acquired as z-stacks with a 1 μm step size and stack sizes ranged between 25-30 μm. Parameters were kept constant for all mice in an experimental group. We define experimental

groups based on the mouse genotype, infection status and the timepoint at which the brain was extracted after infection or sham infection.

Tissue Image Analysis

Images were processed using ImageJ. For image analysis, maximum intensity projections of z-stacks were first obtained. Projected images were thresholded such that GFAP staining in astrocytic cell bodies or Iba-1 staining in microglial cell bodies along with branches (1° and 2°) were masked and ROIs were obtained in this way. In each case, corresponding NeuN labeled or TH labeled sections were processed in a similar manner to astrocytic and microglial staining. Integrated density values were extracted from astrocytic, microglial, and corresponding neuronal components of each slice. Ratios of astrocytic or microglial integrated density to respective neuronal integrated density (NeuN/TH) were obtained. Ratios obtained in this way were averaged across each brain region and all slices for each mouse. By utilizing ratios of glial signal to neuronal staining intensity, we controlled for differences between individual sections that occur due to variations in the efficiency of antibody binding or tissue quality. Data are presented as averages for each mouse. Mean values ± s.e.m. from the averages are presented.

***M. Leprae* Infections**

M. leprae cultivated in the footpads of nude mice was generously provided by the National Hansen's Disease Program. Bacilli were recovered overnight at 33° C, mixed to disperse clumps and resuspended in DMEM supplemented with 10% horse serum. Media were removed from BMDM cells and monolayers overlaid with the bacterial suspension and centrifuged for 10 min at 1000 RPM. Cells were washed twice in PBS and returned to complete media.

Primary Cell Culture

Bone marrow derived macrophages (BMDMs) were differentiated from BM cells isolated by washing mouse femurs with 10ml DMEM. Cells were then centrifuged for 5 min at 1000 rpm and resuspended in BMDM media (DMEM 20% FBS (Millipore) 1mM Sodium pyruvate 10% MCSF conditioned media (Waston lab)). BM cells were counted and plated at $5x10^6$ in 15cm non-TC treated dishes in 30ml complete media. Cells were fed with an additional 15ml of media on day 3. Cells were harvested on day 7 with 1XPBS EDTA. Mouse embryonic fibroblasts (MEFs) were isolated from embryos. Briefly, embryos were dissected from yolk sacs, washed 2 times with cold 1XPBS, decapitated, and peritoneal contents were removed. Headless embryos were

disagreggated in cold 0.05% trypsin-EDTA (Lonza) and incubated on is for 20min. followed by incubation at 37°C for an additional 20min. Cells were then DNAse treated with 4ml dissagregation media (DMEM 10% FBS 100ug/ml DNAse) for 20min at 37C. Supernatants were removed and spun down at 1000rpm for 5min. Cells were resuspended in DMEM 10% FBS, 1mM sodium pyruvate, and plated in 15cm TC treated dishes 1 dish per embryo. MEFs were allowed to expand for 2-3 days before harvest with Trypsin 0.05% EDTA. Mixed glial cultures were differentiated from the brains of neonatal mice as described (Lian 2016 Bio Protoc). Microglial cells were differentiated using complete media DMEM 10%FBS 1mM Sodium pyruvate with 10% MCSF conditioned media. Peritoneal macrophages (PEMS), were elicited by intraperitoneal injection of 1ml 3% Thioglycollate broth (BD) for 4 days prior to harvest. For harvest PEMs were isolated from mice by lavage (1X PBS 4°C) and resuspended in RPMI 1640 media with 20% FBS, 1mM Sodium pyruvate(Lonza) and 2mM L-Glutamine(Lonza). Following overnight incubation at 37°C, cells were washed twice (1X PBS 37°C) to remove non-adherant cells (25%).

Cell lines and Treatments

RAW264.7 LRRK2 KO cells (ATCC® SC-6004™) generated by the MJFF, were obtained from the ATCC and used with wild type control LRRK2 parental RAW 264.7 (ATCC® SC-6003™). To deplete mtDNA RAW264.7 cells were seeded at $2x10^6$ cells/well in 10cM non-TC treated dishes and cultured for 4 days in complete media (DMEM 10%FBS 1mMSodium pyruvate) with 300ng/ml Ethidium bromide or 10uM ddC. Cells were split and harvested with 1X PBS EDTA.

Cell stimulations

BMDMs were plated in 12 well plates at $5X10^5$ cells/well, or 6well plates at $1x10^6$ cells/well. MEFs were plated in 12 well dishes at $3x10^5$ cells/well. PEMs were plated in 24-well flat-bottomed plates (Corning) at $1x10^6$ cells/ well. RAW264.7 cells were plated at $7.5x10^5$ cells/well. Astrocyte cultures were plated at $2.5x10^4$ cells/well in 12 well dishes. Microglia were plated at $5x10^5$ cells/well in 12well plates. Cells were stimulated for 4 hrs with 1μM CLO97, 100ng/ml LPS, 10μM ABT737/10uM OVD-PH, or transfected 1ug/ml ISD, 1ug/ml PolyI:C, 1ug/ml cGAMP with lipofectamine. Cells were transfected for 4hrs with 1uM CpG 2395 with Gene Juice. Cells were stimulated for 2hrs with 10μM DMXAA (RAW cells) 50nM (BMDMs), or 200IU IFNB (BMDMs). Glial cells were stimulated for 8 or 24 Hrs with 800IU IFNB, or supernatants from Mtb infected control BMDMs at a 1:5 dilution.

mRNA Sequensing

RNA was isolated using PureLink RNA mini kits (Ambion) quantified on a Bioanalyzer 2100 (Agilent). PolyA+ PE 100 libraries were sequenced on a HiSeq 4000 at the UC Davis Genome Center DNA Technologies and Expression Analysis Core. Heatmaps were generated by performing Cluster analysis (Cluster3) followed by Java TreeView. Transcriptome analysis was performed using IPA analysis to generate GO term and disease pathway lists. Instant Clue was used to generate scatter plots and volcano plots.

qRT-PCR

RNA was isolated using Directzol RNAeasy kits (Zymogen). cDNA was made with iScript direct synthesis (BioRad) per manufacturers protocol. qRT-PCR was performed in triplicate using Sybr green Power-up (ThermoFisher). Data was analyzed on a ViiA 7 Real-Time PCR System (Applied Biosystems). See extended methods for list of primer sequences.

Cytosolic DNA isolation

MEFs were plated in 10cm dishes at $3x10^6$. The next day, confluent plates were treated as indicated with inhibitors. To harvest, cells were lifted with PBS+EDTA. To determine total DNA content, 1% of the input was saved and processed by adding NaOH to 50 mM, boiling 30 min, and neutralizing with 1:10 1 M Tris pH 8.0. To isolate cytosolic DNA, the cells were pelleted and resuspended in digitonin lysis buffer (150 mM HEPES pH 7.4, 50 mM NaCl, 10 mM EDTA, 25 µg/ml digitonin). Cells were incubated for 15 at 4°C on an end-over-end rotator. Cells were spun at 980 x g for 3 min, and the DNA from the supernatant (cytosolic fraction) was then extracted via phenol:chloroform (1:1 supernatant:phenol/chloroform). The DNA from the aqueous layer was precipitated in 0.3M sodium acetate, 10 mM magnesium chloride, 1µg/ml glycogen, and 75% ethanol. After freezing overnight at -20°C, the DNA was pelleted, washed in 70% ethanol, dried, resuspended in TE, and solubilized at 50°C for 30 min. qPCR was performed on the input (1:50 dilution) and cytosolic (1:2 dilution) samples using nuclear (*Tert*) and mitochondrial (*16s* and *cytB*) genes. The total and cytosolic mitochondrial DNA was normalized to nuclear DNA in order to control for variation in cell number.

Western blot

Cells were washed with PBS and lysed in 1X RIPA buffer with protease and phosphatase inhibitors (Pierce). DNA was degraded using (units) benzonase (EMD Millipore). Proteins were separated by SDS-PAGE and transferred to nitrocellulose membranes. Membranes were

blocked for 1hr RT in Odessy blocking buffer (Licor) Blots were incubated o/n at 4°C with the following Abs. IRF3 (Cell Signaling) 1:1000, pIRF3 Ser396 (Cell Signaling 4947) 1:1000, Iba1 (Wako Chemical 019-19741) 1:2000, Beta Actin 1:5000 (abcam), tubulin 1:5000 (abcam). Membranes were incubated with respective secondary Ab for 2hrs at RT prior to reading on an Odyssey Fc Dual-Mode Imaging System (Licor).

Seahorse metabolic assays

Seahorse XF mito stress test kits and cartridges (Agilent) were prepared per manufacturers protocol as described here (Bossche 2015) and analyzed on a Seahorse XF 96well Analyzer(Agilent). BMDMs were seeded at $5x10^4$ cells/well o/n and treated with 200μM mitoTEMPO, IFNB neutralizing Ab, or Sodium pyruvate at 0mM, 1mM, or 2mM final concentration.

Immuno-multiplex assay

Sera was analyzed by Eve Technologies: Mouse Cytokine Array / Chemokine Array 13-plex Secondary Panel (MD13). Briefly, sera was isolated following decapitation in Microtainer serum separator tubes (BD Biosciences) followed by 2x sterile filtration with Ultrafree-MC sterile fiters, 10min at 10,000rpm (Millipore Sigma). For analysis sera was prediluted 1:1 to a final volume of 100ul in 1xPBS pH 7.4 and assayed/analyzed in duplicate per manufacturer.

Flow cytometry

JC-1 assay to assess mitochondrial membrane potential: Cells were lifted off culture plates with 1X PBS EDTA (BMDMs, RAW264.7 and microglia) or Accutase (Biolegend) (MEFs and Astrocytes). Single cell suspensions were made in 1X PBS 4% FBS. JC-1 dye (ThermoFisher) was sonicated for 5 minutes with 30 second intervals. Cells were stained for 30min at 37°C in 1μM JC-1 dye and analyzed on an LSR Fortessa X20 (BD biosciences). Aggregates were measured under Texas Red (610/20 600LP). monomers were measured under FITC (525/50 505LP). To assess mitochondrial membrane potential under stress, cells were treated for 3 hrs with rotenone 2.5uM prior to being lifted of the culture plates followed by 5uM ATP for 5, 15, and 30 min. For rescue assays cells were treated o/n with mitoTEMPO (Sigma Aldrich) 200uM, or urate (Sigma Aldrich) 100uM.

Phospho-DPR1 assay: Cells were washed once in 1X PBS and Fixed in 4% cold PFA for 10 min cells were then permeabilized with 0.3% Triton-X for 15 minutes followed by 30 min block in

0.1% Triton-X 5% normal rat serum (Stem Cell Technologies). Cells were incubated in pDrp1 Ab o/n at 4°C in 0.1% triton-X 1% BSA. Ab AF488 Goat anti Rabbit were used as secondary antibodies, Cells were analyzed on an LSR Fortessa X20 (BD biosciences). Cells were measured under FITC (525/50 505LP). For rescue and exacerbation assays Cells were treated with H2O2 100μM for 1hr at 37°C or for 12 hrs in the presence of The Drp1 inhibitor Mdivi-1 (50uμM).

LCM/MS/MS

Sample Extraction: Samples were weighed and extracted with a methanol:chloroform:water based extraction method. Briefly 800 uL ice cold methanol:chloroform (1:1, v:v) was added to samples in a bead based lysis tube (Bertin, Rockville, MD). Samples were extracted on a Precyllys 24 (Bertin) tissue homogenizer for 30 seconds at a speed of 6000. The supernatant was collected and samples were homogenized a second time with 800 μL ice methanol:chloroform. 600 μL ice cold water was added to the combined extract, vortexed and centrifuged to separate the phases. The upper aqueous layer was passed through a 0.2 μm nylon filter (Merck Millipore, Burlington, MA). 500 μL of the filtered aqueous phase was then passed through a 3 kDa cutoff column (Thermo Scientific) and the flow through was collected for analysis.

Sample Analysis: Untargeted liquid chromatography high-resolution accurate mass spectrometry (LC-HRAM) analysis was performed on a Q Exactive Plus orbitrap mass spectrometer (Thermo Scientific, Waltham, MA) coupled to a binary pump HPLC (UltiMate 3000, Thermo Scientific). For acquisition the Sheath, Aux and Sweep gasses were set at 50, 15 and 1 respectively. The spray voltage was set to 3.5 kV (Pos) or 2.8 kV (Neg) and the S-lens RF was set to 50. The source and capillary temperatures were maintained at 350°C and 350°C respectively. Full MS spectra were obtained at 70,000 resolution (200 m/z) with a scan range of 50-750 m/z. Full MS followed by ddMS2 scans were obtained at 35,000 resolution (MS1) and 17,500 resolution (MS2) with a 1.5 m/z isolation window and a stepped NCE (20, 40, 60). Samples were maintained at 4 °C before injection. The injection volume was 10 μL. Chromatographic separation was achieved on a Synergi Fusion 4μm, 150 mm x 2 mm reverse phase column (Phenomenex, Torrance, CA) maintained at 30 °C using a solvent gradient method. Solvent A was water (0.1% formic acid). Solvent B was methanol (0.1% formic acid). The gradient method used was 0-5 min (10% B to 40% B), 5-7 min (40% B to 95% B), 7-9 min (95% B), 9-9.1 min (95% B to 10% B), 9.1-13 min (10% B). The flow rate was 0.4 mL min^{-1}.

Sample acquisition was performed Xcalibur (Thermo Scientific). Data analysis was performed with Compound Discoverer 2.1 (Thermo Scientific).

Statistical analysis

All data are representative of 2 or more independent experiments with an n=3 or 4. Graphs were generated using Prism (GraphPad). Significance for assays were determined using a student's two-tailed t test, or a one way ANOVA followed by a Bonferroni's multiple comparisons test for more than two variables, unless otherwise noted. Error bars represent SEM. Statistical tests for brain sections were run in OriginPro 2019. For each experimental group 5-8 mice were utilized. Eight sections per mouse were used for respective antibody combinations 1) GFAP/NeuN 2) Iba-1/NeuN 3) GFAP/TH and 4) Iba-1/TH, for 2 sections per combination. Resulting in a total of 10-16 brain sections, which represent all of the mice within an experimental group. Utilizing the total number of sections as the sample size for each experimental group, we obtained a power of 1. For statistical comparison each experimental group was tested for normal distribution. Normally distributed sets of data were compared using student's two-tailed *t* test, while non-normally distributed data were tested using a two-tailed Mann Whitney's test. Difference were considered statistically significant if $p < 0.05$.

REFERENCES

An, S., Kumar, R., Sheets, E.D., Benkovic, S.J., 2008. Reversible compartmentalization of de novo purine biosynthetic complexes in living cells. Science 320, 103–106. doi:10.1126/science.1152241

Bakshi, R., Macklin, E.A., Logan, R., Zorlu, M.M., Xia, N., Crotty, G.F., Zhang, E., Chen, X., Ascherio, A., Schwarzschild, M.A., 2019. Higher urate in LRRK2 mutation carriers resistant to Parkinson disease. Ann. Neurol. 85, 593–599. doi:10.1002/ana.25436

Balin, B.J., Appelt, D.M., 2001. Role of infection in Alzheimer's disease. J Am Osteopath Assoc 101, S1–6.

Bedford, C., Sears, C., Perez-Carrion, M., Piccoli, G., Condliffe, S.B., 2016. LRRK2 Regulates Voltage-Gated Calcium Channel Function. Front Mol Neurosci 9, 35. doi:10.3389/fnmol.2016.00035

Berry, M.P.R., Graham, C.M., McNab, F.W., Xu, Z., Bloch, S.A.A., Oni, T., Wilkinson, K.A., Banchereau, R., Skinner, J., Wilkinson, R.J., Quinn, C., Blankenship, D., Dhawan, R., Cush, J.J., Mejias, A., Ramilo, O., Kon, O.M., Pascual, V., Banchereau, J., Chaussabel, D., O'Garra, A., 2010. An interferon-inducible neutrophil-driven blood transcriptional signature in human tuberculosis. Nature 466, 973–977. doi:10.1038/nature09247

Calì, T., Ottolini, D., Brini, M., 2014. Calcium signaling in Parkinson's disease. Cell Tissue Res. 357, 439–454. doi:10.1007/s00441-014-1866-0

Chen, X., Wu, G., Schwarzschild, M.A., 2012. Urate in Parkinson's disease: more than a biomarker? Curr Neurol Neurosci Rep 12, 367–375. doi:10.1007/s11910-012-0282-7

Civiero, L., Cogo, S., Biosa, A., Greggio, E., 2018. The role of LRRK2 in cytoskeletal dynamics. Biochem. Soc. Trans. 46, 1653–1663. doi:10.1042/BST20180469

Collins, A.C., Cai, H., Li, T., Franco, L.H., Li, X.-D., Nair, V.R., Scharn, C.R., Stamm, C.E., Levine, B., Chen, Z.J., Shiloh, M.U., 2015. Cyclic GMP-AMP Synthase Is an Innate Immune DNA Sensor for Mycobacterium tuberculosis. Cell Host Microbe 17, 820–828. doi:10.1016/j.chom.2015.05.005

Cookson, M.R., 2017. Mechanisms of Mutant LRRK2 Neurodegeneration. Adv Neurobiol 14, 227–239. doi:10.1007/978-3-319-49969-7_12

Cowan, K., Anichtchik, O., Luo, S., 2019. Mitochondrial integrity in neurodegeneration. CNS Neurosci Ther 25, 825–836. doi:10.1111/cns.13105

De Chiara, G., Marcocci, M.E., Sgarbanti, R., Civitelli, L., Ripoli, C., Piacentini, R., Garaci, E., Grassi, C., Palamara, A.T., 2012. Infectious agents and neurodegeneration. Mol. Neurobiol. 46, 614–638. doi:10.1007/s12035-012-8320-7

de Toledo-Pinto, T.G., Ferreira, A.B.R., Ribeiro-Alves, M., Rodrigues, L.S., Batista-Silva, L.R., Silva, B.J. de A., Lemes, R.M.R., Martinez, A.N., Sandoval, F.G., Alvarado-Arnez, L.E., Rosa, P.S., Shannon, E.J., Pessolani, M.C.V., Pinheiro, R.O., Antunes, S.L.G., Sarno, E.N., Lara, F.A., Williams, D.L., Ozório Moraes, M., 2016. STING-Dependent 2“-5” Oligoadenylate Synthetase-Like Production Is Required for Intracellular Mycobacterium leprae Survival. J. Infect. Dis. 214, 311–320. doi:10.1093/infdis/jiw144

Diner, E.J., Burdette, D.L., Wilson, S.C., Monroe, K.M., Kellenberger, C.A., Hyodo, M., Hayakawa, Y., Hammond, M.C., Vance, R.E., 2013. The innate immune DNA sensor cGAS produces a noncanonical cyclic dinucleotide that activates human STING. Cell Rep 3, 1355–1361. doi:10.1016/j.celrep.2013.05.009

Fava, V.M., Manry, J., Cobat, A., Orlova, M., Van Thuc, N., Ba, N.N., Thai, V.H., Abel, L., Alcaïs, A., Schurr, E., Canadian Lrrk2 in Inflammation Team (CLINT), 2016. A Missense LRRK2 Variant Is a Risk Factor for Excessive Inflammatory Responses in Leprosy. PLoS Negl Trop Dis 10, e0004412. doi:10.1371/journal.pntd.0004412

French, J.B., Jones, S.A., Deng, H., Pedley, A.M., Kim, D., Chan, C.Y., Hu, H., Pugh, R.J.,

Zhao, H., Zhang, Y., Huang, T.J., Fang, Y., Zhuang, X., Benkovic, S.J., 2016. Spatial colocalization and functional link of purinosomes with mitochondria. Science 351, 733–737. doi:10.1126/science.aac6054
Gardet, A., Benita, Y., Li, C., Sands, B.E., Ballester, I., Stevens, C., Korzenik, J.R., Rioux, J.D., Daly, M.J., Xavier, R.J., Podolsky, D.K., 2010. LRRK2 is involved in the IFN-gamma response and host response to pathogens. J. Immunol. 185, 5577–5585. doi:10.4049/jimmunol.1000548
Härtlova, A., Herbst, S., Peltier, J., Rodgers, A., Bilkei-Gorzo, O., Fearns, A., Dill, B.D., Lee, H., Flynn, R., Cowley, S.A., Davies, P., Lewis, P.A., Ganley, I.G., Martinez, J., Alessi, D.R., Reith, A.D., Trost, M., Gutierrez, M.G., 2018. LRRK2 is a negative regulator of Mycobacterium tuberculosis phagosome maturation in macrophages. EMBO J. 37, e98694. doi:10.15252/embj.201798694
Herbst, S., Gutierrez, M.G., 2019. LRRK2 in Infection: Friend or Foe? ACS Infect Dis 5, 809–815. doi:10.1021/acsinfecdis.9b00051
Ho, D.H., Je, A.R., Lee, H., Son, I., Kweon, H.-S., Kim, H.-G., Seol, W., 2018. LRRK2 Kinase Activity Induces Mitochondrial Fission in Microglia via Drp1 and Modulates Neuroinflammation. Exp Neurobiol 27, 171–180. doi:10.5607/en.2018.27.3.171
Ho, D.H., Lee, H., Son, I., Seol, W., 2019. G2019s LRRK2 promotes mitochondrial fission and increases TNFα-mediated neuroinflammation responses. Anim Cells Syst (Seoul) 23, 106–111. doi:10.1080/19768354.2019.1585948
Hsieh, C.-H., Shaltouki, A., Gonzalez, A.E., Bettencourt da Cruz, A., Burbulla, L.F., St Lawrence, E., Schüle, B., Krainc, D., Palmer, T.D., Wang, X., 2016. Functional Impairment in Miro Degradation and Mitophagy Is a Shared Feature in Familial and Sporadic Parkinson's Disease. Cell Stem Cell 19, 709–724. doi:10.1016/j.stem.2016.08.002
Johansen, K.K., Wang, L., Aasly, J.O., White, L.R., Matson, W.R., Henchcliffe, C., Beal, M.F., Bogdanov, M., 2009. Metabolomic profiling in LRRK2-related Parkinson's disease. PLoS ONE 4, e7551. doi:10.1371/journal.pone.0007551
Kasashima, K., Sumitani, M., Endo, H., 2011. Human mitochondrial transcription factor A is required for the segregation of mitochondrial DNA in cultured cells. Exp. Cell Res. 317, 210–220. doi:10.1016/j.yexcr.2010.10.008
Kelly, B., O'Neill, L.A.J., 2015. Metabolic reprogramming in macrophages and dendritic cells in innate immunity. Cell Res. 25, 771–784. doi:10.1038/cr.2015.68
Kett, L.R., Boassa, D., Ho, C.C.-Y., Rideout, H.J., Hu, J., Terada, M., Ellisman, M., Dauer, W.T., 2012. LRRK2 Parkinson disease mutations enhance its microtubule association. Hum. Mol. Genet. 21, 890–899. doi:10.1093/hmg/ddr526
Khakh, B.S., Sofroniew, M.V., 2015. Diversity of astrocyte functions and phenotypes in neural circuits. Nat. Neurosci. 18, 942–952. doi:10.1038/nn.4043
Kim, C.Y., Alcalay, R.N., 2017. Genetic Forms of Parkinson's Disease. Semin Neurol 37, 135–146. doi:10.1055/s-0037-1601567
Leibowitz, R.D., 1971. The effect of ethidium bromide on mitochondrial DNA synthesis and mitochondrial DNA structure in HeLa cells. J. Cell Biol. 51, 116–122. doi:10.1083/jcb.51.1.116
Liang, H.L., Sedlic, F., Bosnjak, Z., Nilakantan, V., 2010. SOD1 and MitoTEMPO partially prevent mitochondrial permeability transition pore opening, necrosis, and mitochondrial apoptosis after ATP depletion recovery. Free Radic. Biol. Med. 49, 1550–1560. doi:10.1016/j.freeradbiomed.2010.08.018
Liu, W., Liu, X., Li, Y., Zhao, J., Liu, Z., Hu, Z., Wang, Y., Yao, Y., Miller, A.W., Su, B., Cookson, M.R., Li, X., Kang, Z., 2017. LRRK2 promotes the activation of NLRC4 inflammasome during Salmonella Typhimurium infection. J. Exp. Med. 214, 3051–3066. doi:10.1084/jem.20170014
López de Maturana, R., Lang, V., Zubiarrain, A., Sousa, A., Vázquez, N., Gorostidi, A., Águila,

J., López de Munain, A., Rodríguez, M., Sánchez-Pernaute, R., 2016. Mutations in LRRK2 impair NF-κB pathway in iPSC-derived neurons. J Neuroinflammation 13, 295. doi:10.1186/s12974-016-0761-x
Manzanillo, P.S., Shiloh, M.U., Portnoy, D.A., Cox, J.S., 2012. Mycobacterium tuberculosis activates the DNA-dependent cytosolic surveillance pathway within macrophages. Cell Host Microbe 11, 469–480. doi:10.1016/j.chom.2012.03.007
Marcinek, P., Jha, A.N., Shinde, V., Sundaramoorthy, A., Rajkumar, R., Suryadevara, N.C., Neela, S.K., van Tong, H., Balachander, V., Valluri, V.L., Thangaraj, K., Velavan, T.P., 2013. LRRK2 and RIPK2 variants in the NOD 2-mediated signaling pathway are associated with susceptibility to Mycobacterium leprae in Indian populations. PLoS ONE 8, e73103. doi:10.1371/journal.pone.0073103
Martin, I., Kim, J.W., Dawson, V.L., Dawson, T.M., 2014. LRRK2 pathobiology in Parkinson's disease. J. Neurochem. 131, 554–565. doi:10.1111/jnc.12949
Meyer, R.R., Simpson, M.V., 1969. DNA biosynthesis in mitochondria. Differential inhibition of mitochondrial and nuclear DNA polymerases by the mutagenic dyes ethidium bromide and acriflavin. Biochem. Biophys. Res. Commun. 34, 238–244. doi:10.1016/0006-291x(69)90637-8
Moehle, M.S., Webber, P.J., Tse, T., Sukar, N., Standaert, D.G., DeSilva, T.M., Cowell, R.M., West, A.B., 2012. LRRK2 inhibition attenuates microglial inflammatory responses. J. Neurosci. 32, 1602–1611. doi:10.1523/JNEUROSCI.5601-11.2012
Ousman, S.S., Kubes, P., 2012. Immune surveillance in the central nervous system. Nat. Neurosci. 15, 1096–1101. doi:10.1038/nn.3161
Panchal, K., Tiwari, A.K., 2019. Mitochondrial dynamics, a key executioner in neurodegenerative diseases. Mitochondrion 47, 151–173. doi:10.1016/j.mito.2018.11.002
Parone, P.A., Da Cruz, S., Tondera, D., Mattenberger, Y., James, D.I., Maechler, P., Barja, F., Martinou, J.-C., 2008. Preventing mitochondrial fission impairs mitochondrial function and leads to loss of mitochondrial DNA. PLoS ONE 3, e3257. doi:10.1371/journal.pone.0003257
Patrick, K.L., Bell, S.L., Weindel, C.G., Watson, R.O., 2019. Exploring the “Multiple-Hit Hypothesis” of Neurodegenerative Disease: Bacterial Infection Comes Up to Bat. Front Cell Infect Microbiol 9, 138. doi:10.3389/fcimb.2019.00138
Pellegrini, L., Wetzel, A., Grannó, S., Heaton, G., Harvey, K., 2017. Back to the tubule: microtubule dynamics in Parkinson's disease. Cell. Mol. Life Sci. 74, 409–434. doi:10.1007/s00018-016-2351-6
Pereira, C., Miguel Martins, L., Saraiva, L., 2014. LRRK2, but not pathogenic mutants, protects against H2O2 stress depending on mitochondrial function and endocytosis in a yeast model. Biochim. Biophys. Acta 1840, 2025–2031. doi:10.1016/j.bbagen.2014.02.015
Perez-Carrion, M., Pischedda, F., Biosa, A., Russo, I., Straniero, L., Civiero, L., Guida, M., Gloeckner, C.J., Ticozzi, N., Tiloca, C., Mariani, C., Pezzoli, G., Duga, S., Pichler, I., Pan, L., Landers, J.E., Greggio, E., Hess, M.W., Goldwurm, S., Piccoli, G., 2018. The LRRK2 Variant E193K Prevents Mitochondrial Fission Upon MPP+ Treatment by Altering LRRK2 Binding to DRP1. Front Mol Neurosci 11, 64. doi:10.3389/fnmol.2018.00064
Russo, I., Kaganovich, A., Ding, J., Landeck, N., Mamais, A., Varanita, T., Biosa, A., Tessari, I., Bubacco, L., Greggio, E., Cookson, M.R., 2019. Transcriptome analysis of LRRK2 knock-out microglia cells reveals alterations of inflammatory- and oxidative stress-related pathways upon treatment with α-synuclein fibrils. Neurobiol. Dis. 129, 67–78. doi:10.1016/j.nbd.2019.05.012
Ryan, B.J., Hoek, S., Fon, E.A., Wade-Martins, R., 2015. Mitochondrial dysfunction and mitophagy in Parkinson's: from familial to sporadic disease. Trends Biochem. Sci. 40, 200–210. doi:10.1016/j.tibs.2015.02.003
Sanna, G., Del Giudice, M.G., Crosio, C., Iaccarino, C., 2012. LRRK2 and vesicle trafficking. Biochem. Soc. Trans. 40, 1117–1122. doi:10.1042/BST20120117

Schendel, F.J., Cheng, Y.S., Otvos, J.D., Wehrli, S., Stubbe, J., 1988. Characterization and chemical properties of phosphoribosylamine, an unstable intermediate in the de novo purine biosynthetic pathway. Biochemistry 27, 2614–2623. doi:10.1021/bi00407a052

Schildt, A., Walker, M.D., Dinelle, K., Miao, Q., Schulzer, M., O'Kusky, J., Farrer, M.J., Doudet, D.J., Sossi, V., 2019. Single Inflammatory Trigger Leads to Neuroinflammation in LRRK2 Rodent Model without Degeneration of Dopaminergic Neurons. Journal of Parkinson's Disease 9, 121–139. doi:10.3233/JPD-181446

Schindelin, J., Arganda-Carreras, I., Frise, E., Kaynig, V., Longair, M., Pietzsch, T., Preibisch, S., Rueden, C., Saalfeld, S., Schmid, B., Tinevez, J.-Y., White, D.J., Hartenstein, V., Eliceiri, K., Tomancak, P., Cardona, A., 2012. Fiji: an open-source platform for biological-image analysis. Nat. Methods 9, 676–682. doi:10.1038/nmeth.2019

Schoggins, J.W., MacDuff, D.A., Imanaka, N., Gainey, M.D., Shrestha, B., Eitson, J.L., Mar, K.B., Richardson, R.B., Ratushny, A.V., Litvak, V., Dabelic, R., Manicassamy, B., Aitchison, J.D., Aderem, A., Elliott, R.M., García-Sastre, A., Racaniello, V., Snijder, E.J., Yokoyama, W.M., Diamond, M.S., Virgin, H.W., Rice, C.M., 2014. Pan-viral specificity of IFN-induced genes reveals new roles for cGAS in innate immunity. Nature 505, 691–695. doi:10.1038/nature12862

Schulz, J.B., Hausmann, L., Hardy, J., 2016. 199 years of Parkinson disease - what have we learned and what is the path to the future? J. Neurochem. 139 Suppl 1, 3–7. doi:10.1111/jnc.13733

Shen, C.-H., Chou, C.-H., Liu, F.-C., Lin, T.-Y., Huang, W.-Y., Wang, Y.-C., Kao, C.-H., 2016. Association Between Tuberculosis and Parkinson Disease: A Nationwide, Population-Based Cohort Study. Medicine (Baltimore) 95, e2883. doi:10.1097/MD.0000000000002883

Shi, M.-M., Shi, C.-H., Xu, Y.-M., 2017. Rab GTPases: The Key Players in the Molecular Pathway of Parkinson's Disease. Front Cell Neurosci 11, 81. doi:10.3389/fncel.2017.00081

Singh, A., Zhi, L., Zhang, H., 2019. LRRK2 and mitochondria: Recent advances and current views. Brain Res. 1702, 96–104. doi:10.1016/j.brainres.2018.06.010

Sison, S.L., Vermilyea, S.C., Emborg, M.E., Ebert, A.D., 2018. Using Patient-Derived Induced Pluripotent Stem Cells to Identify Parkinson's Disease-Relevant Phenotypes. Curr Neurol Neurosci Rep 18, 84. doi:10.1007/s11910-018-0893-8

Sliter, D.A., Martinez, J., Hao, L., Chen, X., Sun, N., Fischer, T.D., Burman, J.L., Li, Y., Zhang, Z., Narendra, D.P., Cai, H., Borsche, M., Klein, C., Youle, R.J., 2018. Parkin and PINK1 mitigate STING-induced inflammation. Nature 561, 258–262. doi:10.1038/s41586-018-0448-9

Smith, G.A., Jansson, J., Rocha, E.M., Osborn, T., Hallett, P.J., Isacson, O., 2016. Fibroblast Biomarkers of Sporadic Parkinson's Disease and LRRK2 Kinase Inhibition. Mol. Neurobiol. 53, 5161–5177. doi:10.1007/s12035-015-9435-4

Srinivasan, R., Huang, B.S., Venugopal, S., Johnston, A.D., Chai, H., Zeng, H., Golshani, P., Khakh, B.S., 2015. Ca(2+) signaling in astrocytes from Ip3r2(-/-) mice in brain slices and during startle responses in vivo. Nat. Neurosci. 18, 708–717. doi:10.1038/nn.4001

Srinivasan, R., Lu, T.-Y., Chai, H., Xu, J., Huang, B.S., Golshani, P., Coppola, G., Khakh, B.S., 2016. New Transgenic Mouse Lines for Selectively Targeting Astrocytes and Studying Calcium Signals in Astrocyte Processes In Situ and In Vivo. Neuron 92, 1181–1195. doi:10.1016/j.neuron.2016.11.030

Stephens, B., Mueller, A.J., Shering, A.F., Hood, S.H., Taggart, P., Arbuthnott, G.W., Bell, J.E., Kilford, L., Kingsbury, A.E., Daniel, S.E., Ingham, C.A., 2005. Evidence of a breakdown of corticostriatal connections in Parkinson's disease. Neuroscience 132, 741–754. doi:10.1016/j.neuroscience.2005.01.007

Su, Y.-C., Qi, X., 2013. Inhibition of excessive mitochondrial fission reduced aberrant autophagy and neuronal damage caused by LRRK2 G2019S mutation. Hum. Mol. Genet. 22, 4545–4561. doi:10.1093/hmg/ddt301

Surmeier, D.J., Obeso, J.A., Halliday, G.M., 2017. Selective neuronal vulnerability in Parkinson disease. Nat. Rev. Neurosci. 18, 101–113. doi:10.1038/nrn.2016.178
Taguchi, N., Ishihara, N., Jofuku, A., Oka, T., Mihara, K., 2007. Mitotic phosphorylation of dynamin-related GTPase Drp1 participates in mitochondrial fission. J. Biol. Chem. 282, 11521–11529. doi:10.1074/jbc.M607279200
Tanner, C.M., Kamel, F., Ross, G.W., Hoppin, J.A., Goldman, S.M., Korell, M., Marras, C., Bhudhikanok, G.S., Kasten, M., Chade, A.R., Comyns, K., Richards, M.B., Meng, C., Priestley, B., Fernandez, H.H., Cambi, F., Umbach, D.M., Blair, A., Sandler, D.P., Langston, J.W., 2011. Rotenone, paraquat, and Parkinson's disease. Environ. Health Perspect. 119, 866–872. doi:10.1289/ehp.1002839
Umeno, J., Asano, K., Matsushita, T., Matsumoto, T., Kiyohara, Y., Iida, M., Nakamura, Y., Kamatani, N., Kubo, M., 2011. Meta-analysis of published studies identified eight additional common susceptibility loci for Crohn's disease and ulcerative colitis. Inflamm. Bowel Dis. 17, 2407–2415. doi:10.1002/ibd.21651
Van Limbergen, J., Wilson, D.C., Satsangi, J., 2009. The genetics of Crohn's disease. Annu Rev Genomics Hum Genet 10, 89–116. doi:10.1146/annurev-genom-082908-150013
Villalba, R.M., Lee, H., Smith, Y., 2009. Dopaminergic denervation and spine loss in the striatum of MPTP-treated monkeys. Exp. Neurol. 215, 220–227. doi:10.1016/j.expneurol.2008.09.025
Wang, D., Xu, L., Lv, L., Su, L.-Y., Fan, Y., Zhang, D.-F., Bi, R., Yu, D., Zhang, W., Li, X.-A., Li, Y.-Y., Yao, Y.-G., 2015. Association of the LRRK2 genetic polymorphisms with leprosy in Han Chinese from Southwest China. Genes Immun. 16, 112–119. doi:10.1038/gene.2014.72
Wang, X., Yan, M.H., Fujioka, H., Liu, J., Wilson-Delfosse, A., Chen, S.G., Perry, G., Casadesus, G., Zhu, X., 2012. LRRK2 regulates mitochondrial dynamics and function through direct interaction with DLP1. Hum. Mol. Genet. 21, 1931–1944. doi:10.1093/hmg/dds003
Wassermann, R., Gulen, M.F., Sala, C., Perin, S.G., Lou, Y., Rybniker, J., Schmid-Burgk, J.L., Schmidt, T., Hornung, V., Cole, S.T., Ablasser, A., 2015. Mycobacterium tuberculosis Differentially Activates cGAS- and Inflammasome-Dependent Intracellular Immune Responses through ESX-1. Cell Host Microbe 17, 799–810. doi:10.1016/j.chom.2015.05.003
Watson, R.O., Bell, S.L., MacDuff, D.A., Kimmey, J.M., Diner, E.J., Olivas, J., Vance, R.E., Stallings, C.L., Virgin, H.W., Cox, J.S., 2015. The Cytosolic Sensor cGAS Detects Mycobacterium tuberculosis DNA to Induce Type I Interferons and Activate Autophagy. Cell Host Microbe 17, 811–819. doi:10.1016/j.chom.2015.05.004
Watson, R.O., Manzanillo, P.S., Cox, J.S., 2012. Extracellular M. tuberculosis DNA targets bacteria for autophagy by activating the host DNA-sensing pathway. Cell 150, 803–815. doi:10.1016/j.cell.2012.06.040
West, A.P., Khoury-Hanold, W., Staron, M., Tal, M.C., Pineda, C.M., Lang, S.M., Bestwick, M., Duguay, B.A., Raimundo, N., MacDuff, D.A., Kaech, S.M., Smiley, J.R., Means, R.E., Iwasaki, A., Shadel, G.S., 2015. Mitochondrial DNA stress primes the antiviral innate immune response. Nature 520, 553–557. doi:10.1038/nature14156
Wiens, K.E., Ernst, J.D., 2016. The Mechanism for Type I Interferon Induction by Mycobacterium tuberculosis is Bacterial Strain-Dependent. PLoS Pathog. 12, e1005809. doi:10.1371/journal.ppat.1005809
Yang, S., Xia, C., Li, S., Du, L., Zhang, L., Hu, Y., 2014. Mitochondrial dysfunction driven by the LRRK2-mediated pathway is associated with loss of Purkinje cells and motor coordination deficits in diabetic rat model. Cell Death Dis 5, e1217. doi:10.1038/cddis.2014.184
Yue, M., Hinkle, K.M., Davies, P., Trushina, E., Fiesel, F.C., Christenson, T.A., Schroeder, A.S., Zhang, L., Bowles, E., Behrouz, B., Lincoln, S.J., Beevers, J.E., Milnerwood, A.J., Kurti, A.,

McLean, P.J., Fryer, J.D., Springer, W., Dickson, D.W., Farrer, M.J., Melrose, H.L., 2015. Progressive dopaminergic alterations and mitochondrial abnormalities in LRRK2 G2019S knock-in mice. Neurobiol. Dis. 78, 172–195. doi:10.1016/j.nbd.2015.02.031

Zaja-Milatovic, S., Milatovic, D., Schantz, A.M., Zhang, J., Montine, K.S., Samii, A., Deutch, A.Y., Montine, T.J., 2005. Dendritic degeneration in neostriatal medium spiny neurons in Parkinson disease. Neurology 64, 545–547. doi:10.1212/01.WNL.0000150591.33787.A4

Zhang, F.-R., Huang, W., Chen, S.-M., Sun, L.-D., Liu, H., Li, Y., Cui, Y., Yan, X.-X., Yang, H.-T., Yang, R.-D., Chu, T.-S., Zhang, C., Zhang, L., Han, J.-W., Yu, G.-Q., Quan, C., Yu, Y.-X., Zhang, Z., Shi, B.-Q., Zhang, L.-H., Cheng, H., Wang, C.-Y., Lin, Y., Zheng, H.-F., Fu, X.-A., Zuo, X.-B., Wang, Q., Long, H., Sun, Y.-P., Cheng, Y.-L., Tian, H.-Q., Zhou, F.-S., Liu, H.-X., Lu, W.-S., He, S.-M., Du, W.-L., Shen, M., Jin, Q.-Y., Wang, Y., Low, H.-Q., Erwin, T., Yang, N.-H., Li, J.-Y., Zhao, X., Jiao, Y.-L., Mao, L.-G., Yin, G., Jiang, Z.-X., Wang, X.-D., Yu, J.-P., Hu, Z.-H., Gong, C.-H., Liu, Y.-Q., Liu, R.-Y., Wang, D.-M., Wei, D., Liu, J.-X., Cao, W.-K., Cao, H.-Z., Li, Y.-P., Yan, W.-G., Wei, S.-Y., Wang, K.-J., Hibberd, M.L., Yang, S., Zhang, X.-J., Liu, J.-J., 2009. Genomewide association study of leprosy. N. Engl. J. Med. 361, 2609–2618. doi:10.1056/NEJMoa0903753

Zhang, Y., Chen, K., Sloan, S.A., Bennett, M.L., Scholze, A.R., O'Keeffe, S., Phatnani, H.P., Guarnieri, P., Caneda, C., Ruderisch, N., Deng, S., Liddelow, S.A., Zhang, C., Daneman, R., Maniatis, T., Barres, B.A., Wu, J.Q., 2014. An RNA-sequencing transcriptome and splicing database of glia, neurons, and vascular cells of the cerebral cortex. J. Neurosci. 34, 11929–11947. doi:10.1523/JNEUROSCI.1860-14.2014

Zhao, H., French, J.B., Fang, Y., Benkovic, S.J., 2013. The purinosome, a multi-protein complex involved in the de novo biosynthesis of purines in humans. Chem. Commun. (Camb.) 49, 4444–4452. doi:10.1039/c3cc41437j

Zhou, B., Xiao, J.F., Tuli, L., Ressom, H.W., 2012. LC-MS-based metabolomics. Mol Biosyst 8, 470–481. doi:10.1039/c1mb05350g